Airborne Doppler Observations of the Inner-Core Structural Differences between Intensifying and Steady-State Tropical Cyclones

ROBERT ROGERS AND PAUL REASOR

NOAA/AOML/Hurricane Research Division, Miami, Florida

SYLVIE LORSOLO

Cooperative Institute for Marine and Atmospheric Studies, University of Miami, Miami, Florida

ABSTRACT

Differences in the inner-core structure of intensifying [IN; intensity increase of at least $20\,\mathrm{kt}\,(24\,\mathrm{h})^{-1}$, where $1\,\mathrm{kt} = 0.51\,\mathrm{m}\,\mathrm{s}^{-1}$] and steady-state [SS; intensity remaining between $\pm10\,\mathrm{kt}\,(24\,\mathrm{h})^{-1}$] tropical cyclones (TCs) are examined using composites of airborne Doppler observations collected from NOAA P-3 aircraft missions. The IN dataset contains 40 eyewall passes from 14 separate missions, while the SS dataset contains 53 eyewall passes from 14 separate missions. Intensifying TCs have a ringlike vorticity structure inside the radius of maximum wind (RMW); lower vorticity in the outer core; a deeper, stronger inflow layer; and stronger axisymmetric eyewall upward motion compared with steady-state TCs. There is little difference in the vortex tilt between 2 and 7 km, and both IN and SS TCs show an eyewall precipitation and updraft asymmetry whose maxima are located in the downshear and downshear-left region. The azimuthal coverage of eyewall and outer-core precipitation is greater for IN TCs. There is little difference in the distribution of downdrafts and weak to moderate updrafts in the eyewall. The primary difference is seen at the high end of the vertical velocity spectrum, where IN TCs have a larger number of convective bursts. These bursts accomplish more vertical mass flux, but they compose such a small portion of the total vertical velocity distribution that there is little difference in the shape of the net mass flux profile. The radial location of convective bursts for IN TCs is preferentially located inside the RMW, where the axisymmetric vorticity is generally higher, whereas for SS TCs the bursts are located outside the RMW.

1. Introduction

The challenge of predicting tropical cyclone (TC) intensity change remains a top priority for the TC research and forecasting communities. Despite advances in the accuracy of TC track forecasts, progress in intensity forecasts remains limited (Rogers et al. 2006, 2013; DeMaria et al. 2005). The multiscale nature of the processes responsible for intensity change is thought to be a large reason for the relative lack of progress (Marks and Shay 1998).

For extreme cases of TC intensification [i.e., rapid intensification (RI), defined as an increase in the peak

10-m winds of 30 kt in 24 h, where $1\,\mathrm{kt} = 0.51\,\mathrm{m}\,\mathrm{s}^{-1}$] one of the more reliable forecast tools currently used is the rapid intensification index (RII; Kaplan et al. 2010). The RII uses environmental-scale predictors from the Statistical Hurricane Intensity Prediction Scheme (SHIPS; DeMaria and Kaplan 1999), along with a few measures of convective characteristics derived from satellite imagery, to estimate the probability of RI over the succeeding 24 h using linear discriminant analysis. Even though this forecasting tool is currently considered the best at predicting RI, the forecasting skill of the RII still has room for improvement. For example, the Peirce skill score (PSS), which measures the difference between the probability of detection and false alarm ratio (where a value of 1 is a perfect forecast and values less than 0 indicate forecasts that have no skill), was 0.35 for the RII for cases from the 2006 and 2007 seasons (cf. Fig. 17c in Kaplan et al. 2010). Improvements in forecast skill, either through

more forecast "hits" or a reduced number of false alarms, would increase PSS. The remainder of this improvement in skill for RI forecasts, and TC intensity forecasts more broadly, is thought to lie either in smaller-scale processes (i.e., vortex, convective, turbulent, microphysical scale) or be limited by predictability constraints. How much of that remaining forecasting skill can be explained by considering smaller-scale processes and how much is ultimately limited by predictability constraints is unknown at this time. The potential importance of inner-core structure to TC intensification was also discussed in Hendricks et al. (2010), who noted that rapid intensification may be controlled by storm internal dynamics, providing a favorable preexisting environmental condition exists.

Much research has focused on identifying vortex- and convective-scale properties related to TC intensity change. The approach taken usually focuses either on the symmetric characteristics of the vortex structure, the asymmetric characteristics, or the structure of convective-scale features. The cooperative interaction between the symmetric primary and secondary circulation patterns has long been known to be important in TC intensity change (e.g., Ooyama 1969, 1982; Schubert and Hack 1982). Nolan and Grasso (2003) and Nolan et al. (2007) showed that it is the projection of diabatic heating from convection onto the symmetric component that dominates over asymmetric forcing in intensifying a TC. They also identified symmetric properties of the vortex that are associated with intensification, including the strength, vertical structure, and latitude of the vortex.

Other work has focused on the role of asymmetric processes in TC intensity change. Montgomery and Kallenbach (1997) showed that vortex Rossby waves intensify the axisymmetric primary circulation by axisymmetrizing convectively generated potential vorticity perturbations near the radius of maximum winds. Mesovortices are other asymmetric features that have been identified as being important for TC intensity change by mixing momentum, vorticity, and high-entropy air between the eye and eyewall (Schubert et al. 1999; Kossin and Schubert 2001; Montgomery et al. 2002; Persing and Montgomery 2003; Cram et al. 2007). Kossin and Eastin (2001) examined radial profiles of flight-level tangential wind from radial penetrations over a 20-yr period and found that intensifying TCs were characterized by angular velocity that is greatest in the eyewall (where vorticity mixing across the eye–eyewall interface is greatest), while TCs that had already reached their peak intensity had angular velocity maxima that were greatest at the eye center. Nguyen et al. (2011) identified cycles of symmetric–asymmetric transition within the eyewall that were related to periodic intensification of their simulated

TC. The symmetric-to-asymmetric transition of the eyewall was initiated by barotropic–convective instability. Following the weakening of deep convective anomalies and the axisymmetrization of convectively generated vorticity, the storm would intensify. They termed these cycles of structure change vacillation cycles, and suggested that they may be a common phenomenon during the early stages of TC intensification.

The role of convective-scale processes in TC intensity change has received a great deal of attention in the literature. The presence of convective bursts, that is, locations of deep, vigorous convection characterized by cold and expanding cloud tops, ice scattering, frequent lightning, and towers of high reflectivity (Cecil et al. 2002), have been identified as being associated both with tropical cyclogenesis and RI (Houze et al. 2009; Reasor et al. 2009; Squires and Businger 2008; Hennon 2006; Kelley et al. 2004; Rodgers et al. 1998; Gentry et al. 1970). The exact role that these bursts play has been tied to warming from upper-level subsidence around the periphery of the bursts (Chen and Zhang 2013; Zhang and Chen 2012; Guimond et al. 2010; Heymsfield et al. 2001) and to the stretching and subsequent axisymmetrization of low-level vorticity collocated with the updraft in vortical hot towers (VHTs; Houze et al. 2009; Reasor et al. 2009; Montgomery et al. 2006; Hendricks et al. 2004).

Convection and its role in intensification have also been approached from a vertical mass flux perspective. Malkus and Riehl (1960), Simpson et al. (1998), and Braun (2002, 2006) identified hot towers (also called convective bursts) as accomplishing a significant portion of the vertical mass flux in the eyewall. This perspective contrasts with those advanced by Emanuel (1986) and Rotunno and Emanuel (1987), who theorized that TC maintenance and intensification occurred in a state of near-symmetric neutrality, and intensification is driven by an air–sea interaction instability rather than penetrative convection supported by local buoyancy (Smith et al. 2005). Evidence that both approaches are important was found by two studies. The first, by Eastin et al. (2005), examined flight-level data from a multitude of eyewall penetrations and found that eyewall vertical motion was a combination of both buoyantly driven updrafts and slantwise-neutral ascent. Buoyant convective updrafts, however, were integral components of the hurricanes' transverse circulation. The other study was by Rogers (2010), who performed a high-resolution simulation of the RI of Hurricane Dennis (2005), finding that RI was not tied to a dramatic increase in the number of convective bursts nor in the characteristics of the bursts, such as burst intensity. Rather, the immediate cause of RI was a significant increase in updraft mass

flux, particularly in the lowest 1.5 km. This increase in updraft mass flux was accomplished primarily by updrafts on the order of $1-2$ m s^{-1}, representing the bulk of the vertical motion distribution. However, a period of enhanced updraft mass flux in the midlevels by moderate to strong updrafts located inside the radius of maximum winds occurred 6 h prior to RI, indicating a synergistic relationship between convective bursts and the background secondary circulation prior to RI. This result supports the assertion that both buoyantly driven updrafts and slantwise near-neutral ascent are important features in eyewall structure, evolution, and intensification, including RI.

In a study of 10 yr of Tropical Rainfall Measuring Mission (TRMM) data, Jiang (2012) found statistically significant differences in three out of four convective intensity parameters in the inner core exist between RI and non-RI storms, indicating that a relationship does exist between inner-core convective intensity and TC intensity change. However, the increase in the probability of a TC intensifying when hot towers are present in the inner core is not significant, suggesting that hot towers are neither a necessary nor a sufficient condition for RI. This result is consistent with recent work emphasizing the importance of a ring of precipitation in 37-GHz images that highlights rainfall and weak to moderate updrafts rather than ice scattering from deep convection (e.g., Kieper and Jiang 2012).

In addition to examining the relative importance of deep convection versus moderate-strength precipitation in TC intensification, other studies have looked at the importance of the location of the precipitation and the vortex in which it is embedded. Vigh and Schubert (2009) and Pendergrass and Willoughby (2009), using balance models, emphasized that the response of a vortex to diabatic heating is dependent on the radial location of the heating relative to the radius of maximum wind, the strength of the storm itself, and the horizontal and vertical extents of the circulation. These characteristics determine the efficiency with which diabatic heating released within the storm core is converted into an increase in the kinetic energy of the storm (Nolan et al. 2007; Schubert and Hack 1982).

From the above discussion it is clear that there are many aspects of TC inner-core structure that may play a significant role in determining whether or not a TC will intensify. The goal of this research is to identify whether there are detectable differences that exist between the vortex- and convective-scale structures of TCs that intensify and those that do not intensify. While individual case studies have been performed to identify characteristics of TCs that intensify (e.g., Heymsfield et al. 2001; Reasor et al. 2009, 2013; Guimond et al. 2010),

a composite approach is followed here. Composites of the inner-core structure of TCs from airborne Doppler radar data collected on board National Oceanic and Atmospheric Administration (NOAA) WP-3D aircraft over an 11-yr period are compared for two datasets: intensifying and steady-state TCs. Such an approach provides a measure of the robustness of any differences that are detected between the two datasets. This composite methodology has been shown to produce a realistic representation of axisymmetric and convective-scale structures of mature TCs (Rogers et al. 2012) and captures the asymmetric structure of TCs encountering vertical shear (Reasor et al. 2013). It is hoped that by identifying differences in the inner-core structure of intensifying versus steady-state TCs, information from future aircraft missions in TCs can be used to explain some of the remaining 65% of the forecast skill uncertainty mentioned above, and the short-term (e.g., 6–24 h) forecast of TC intensity can be improved.

2. Methodology

a. Description of dataset

The analyses used here rely on an automated variational synthesis (Gamache 1997) of reflectivity and Doppler radial velocity. The wind analyses produced are a global three-dimensional variational solution of the continuity and Doppler projection equations, similar to what was done in Gao et al. (1999) and Reasor et al. (2009), and they are obtained from radial legs flown by the NOAA WP-3D aircraft. The length of each radial leg (end point to storm center) ranges from ~120 to 180 km, so the total along-track distance for each leg is ~(240–360) km. A three-dimensional Cartesian grid with a horizontal grid spacing of 2×2 km^2 and a vertical spacing of 0.5 km is used here. The domain size of the gridded analyses is 400×400 km^2, though the areal coverage of the data is generally much less than this because of the availability of scatterers, automated quality control, and attenuation. The fall speed is removed before interpolating the Doppler radial observations to produce the gridded solution. To perform azimuthal Fourier analysis, the Cartesian data are mapped to a cylindrical coordinate system centered on the vortex at 2-km altitude with 2-km radial grid spacing. Following Reasor and Eastin (2012), the vortex center is defined using a modified version of the center-finding method of Marks et al. (1992), where the center is chosen to maximize the tangential wind within an annulus centered on the radius of maximum wind (RMW), carefully accounting for gaps in the wind field.

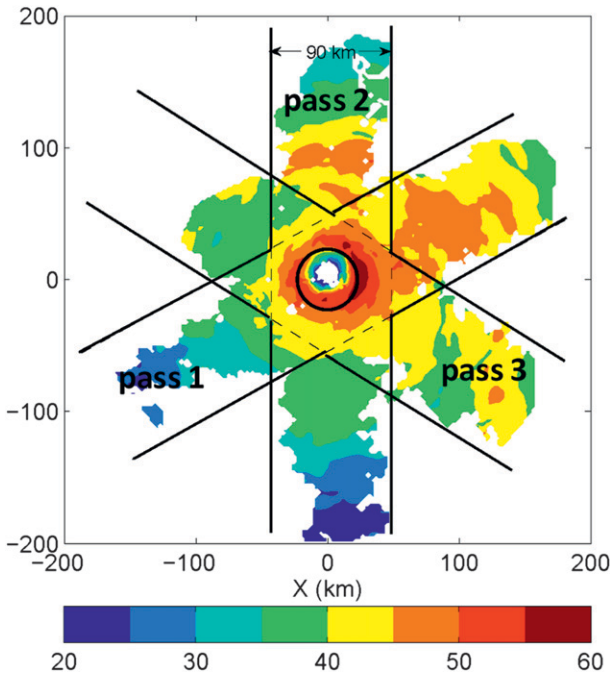The WP-3D flight patterns used for this study consist primarily of a series of radial legs separated by a uniform

FIG. 1. Example of wind speed (color shaded, m s^{-1}) at 2-km altitude for an IOP during Hurricane Earl centered at 0000 UTC 30 Aug 2010. The IOP shown here consists of a merger of three individual radial passes separated by 60°.

TABLE 1. List of storms sampled, dates flown, individual radar passes, and merged analyses from an entire flight (termed IOPs) for (top) IN and (bottom) SS datasets.

IN			
Storm name	Date	No. of passes	No. of IOPs
Ophelia	13 Sep 2005	2	1
Gustav	29–30 Aug 2008	4	2
Earl	29 Aug–1 Sep 2010	13	4
Ivan	7 Sep 2004	4	1
Paloma	7 Nov 2008	8	2
Guillermo	2 Aug 1997	4	2
Felix	1 Sep 2007	2	1
Katrina	27 Aug 2005	3	1
SS			
Storm name	Date	No. of passes	No. of IOPs
Gustav	31 Aug 2008	10	2
Frances	30 Aug–4 Sep 2004	8	3
Ophelia	11 Sep 2005	2	1
Ivan	14 Sep 2004	6	1
Jeanne	24 Sep 2004	6	2
Ike	10–12 Sep 2008	19	4

angular distance (e.g., 90°, 60°, or 45°), with each leg taking ~45 min to complete, depending on the length of the leg. An example of radar data collected from one such flight in Hurricane Earl (2010) is shown in Fig. 1. To maximize the areal coverage, data from all legs during a given flight are merged to form an intensive observing period (IOP). The merger involves a simple average of wind and reflectivity at overlapping storm-relative grid points. Mergers are only used for those structural features that evolve on time scales longer than the time scale of the IOP (generally 3–4 h). A comparison of symmetric and asymmetric vortex-scale structural metrics for the individual swaths and IOP shown in Fig. 1 was performed (not shown). It was found that the metrics are generally consistent indicating these structures are quasi-steady during the time spanned by the IOP and the merged analysis is an appropriate dataset to use for vortex-scale parameters. For analyses of the convective-scale fields, however, which evolve over much shorter time scales, the individual radial passes are used.

b. Selection of cases for each database

Two databases are constructed: one that includes TCs that are intensifying and another that includes TCs that are remaining steady state. The definitions of "intensifying" and "steady state" are based on the peak 10-m

winds of the TC obtained from the best-track (BT) database at the time closest to the IOP. With that time identified, the BT intensity 12 h afterward is examined. If the corresponding intensification rate during this 12-h period is ≥20 kt (24 h)$^{-1}$, then that IOP is classified as being taken from an intensifying (IN) TC. If the corresponding intensification rate is between −10 and 10 kt (24 h)$^{-1}$ (inclusive), then that IOP is classified as being taken from a steady-state (SS) TC. The ensuing 12 h from the IOP time was considered instead of the ensuing 24 h to try to better isolate time scales likely to be most relevant for vortex- and convective-scale processes. A longer time window (e.g., 24 h) provides more of an opportunity for environmental interactions, such as vertical shear and dry air, to impact the TC intensity and obscure a possible signal. Also, no consideration was made for the BT intensity prior to the IOP. Therefore, some cases in the IN database are already undergoing intensification at the time of the IOP, while other cases have yet to begin to intensify. While it would be optimal to consider only TCs that begin to intensify at the time of the IOP, there were not enough cases in the Doppler database to allow such a stratification.

Table 1 shows a list of the cases included in each database. For the IN database a total of 40 eyewall passes from 14 IOPs in eight separate TCs were included. For the SS database there were 53 eyewall passes from 14 IOPs in six separate TCs. A plot of the BT intensity from 48 h prior to 24 h after each IOP is shown in Fig. 2. While there is a spread in the intensity evolution within each database, the general evolution for each IOP is consistent
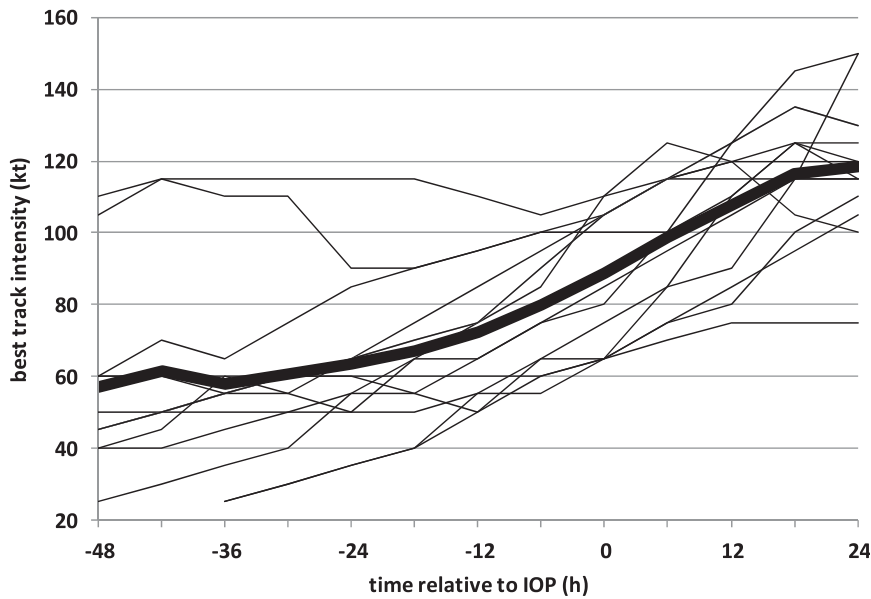
(a)
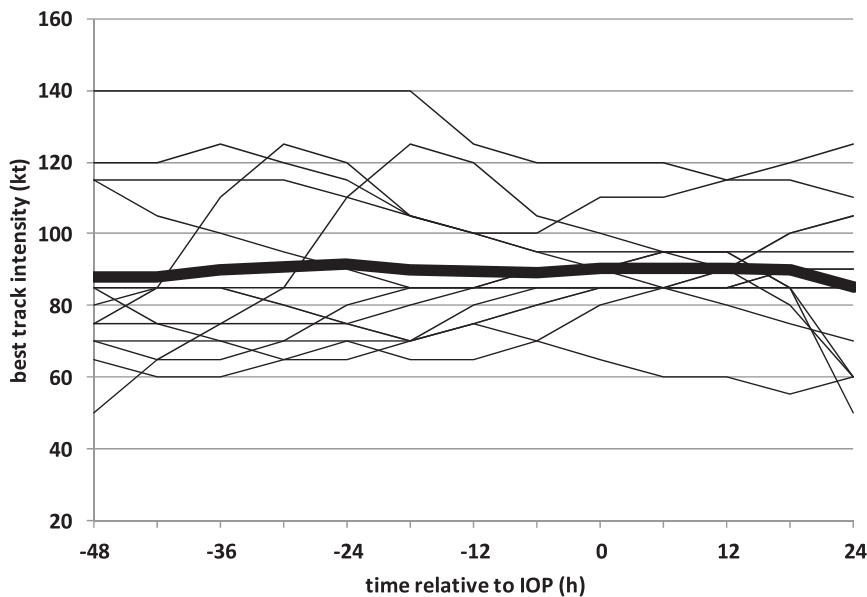
(b)

FIG. 2. Intensity traces from BT data plotted relative to the sampling time for each of 14 IOPs (thin lines) for (a) intensifying and (b) steady-state tropical cyclones. Thick lines in (a) and (b) denote the average intensity trace for each dataset.

with each category. For the IN database there are some cases that are intensifying by $20 \, \mathrm{kt} \, (24 \, \mathrm{h})^{-1}$, but there are others undergoing RI [i.e., with an intensification rate greater than or equal to $30 \, \mathrm{kt} \, (24 \, \mathrm{h})^{-1}$]. In fact, the mean intensity trace for the IN database increases from an average of $\sim 90 \, \mathrm{kt}$ at the time of the IOP to an average of $\sim 120 \, \mathrm{kt}$ at IOP + 24 h, which meets the RI threshold.

Nevertheless, since the intensity change criterion for inclusion of an IOP in the IN database is only $20 \, \mathrm{kt} \, (24 \, \mathrm{h})^{-1}$, the RI label is not used here.

Other criteria are used to determine inclusion in the IN and SS databases. The TC must be at hurricane strength; thus, no tropical storms or tropical depressions are included. This was to ensure that the TC had

TABLE 2. Summary statistics comparing various environmental and vortex parameters for intensifying and steady-state tropical cyclones. Statistics shown include mean, standard deviation, and t statistic. Maximum significance level exceeded using one-sided Student's t test shown. Values that are boldfaced denote differences in the mean that are significant at the $\geq 95\%$ confidence level. The N/A denotes differences that are not statistically significant at any meaningful level.

	IN		SS			Significance
	Mean	Std dev	Mean	Std dev	t statistic	level (%)
Intensification rate (kt h^{-1})	**1.58**	0.66	**0.00**	0.37	7.847	>99
IOP best-track intensity (kt)	88.6	18.9	90.4	13.2	−0.290	N/A
RMW (km)	43.0	23.6	52.5	19.8	−1.153	<90
850–200-hPa shear magnitude from SHIPS (kt)	11.2	5.4	12.3	5.5	−0.538	N/A
850–500-hPa shear magnitude from SHIPS (kt)	**5.0**	3.0	**8.0**	4.4	−2.103	95
Difference between 850- and 200-hPa SHIPS shear vector and storm motion vector (°)	**74.8**	42.2	**107.6**	47.6	−1.923	95
Sea surface temperature from SHIPS (°C)	**29.5**	0.5	**29.2**	0.6	1.811	95

sufficiently well-developed primary and secondary circulation patterns to facilitate compositing across cases. The TC also had to be at least 25 kt below its maximum potential intensity, as defined by the SHIPS database. This was to ensure that each TC had a chance (at least thermodynamically) of intensifying over the next 12 h. TCs included in the database also had to be at least 100 km from land, and there had to be data extending out to at least $1.5 \times$ RMW.

c. Construction of composites and method of comparison

With the IN and SS databases constructed, composites were calculated. The compositing methodology follows that of Rogers et al. (2012). The horizontal dimension of each analysis is scaled by the radius of the maximum axisymmetric wind at 2-km altitude (RMW$_{2km}$). The normalized radius $r*$ is defined by r/RMW$_{2km}$, while the normalized Cartesian coordinates ($x*, y*$) are defined by (x, y)/RMW$_{2km}$. To ensure a common reference center for the compositing, the Cartesian and cylindrical domains of each analysis are defined with their origins at the 2-km vortex center. No attempt was made to account for the slope of the eyewall with height; a comparison of composites accounting for eyewall slope and neglecting eyewall slope (Rogers et al. 2012) yielded no appreciable differences in the mean and variance of the vortex structure within those composites. Student's t tests were performed on select aspects of the various fields to determine whether the composite-mean structures are different from each other at various confidence levels (i.e., 90%, 95%, and 99%).

3. Vortex structure

a. Basic vortex and environmental characteristics

Table 2 shows the values of select parameters for IN and SS storms obtained from the BT and SHIPS

databases. The mean intensification rate for IN storms is ~ 2 kt h^{-1}, whereas the intensification rate for SS storms is ~ 0 kt h^{-1}. The BT intensity for IN storms at the IOP time is 88.6 kt, while the intensity for SS storms is 90.4 kt, indicating that, on average, for both databases the TCs are category 2 hurricanes on the Saffir–Simpson scale at the time of the IOP. However, as seen from Fig. 2, there is a scatter in the IOP intensities within each database. This is also reflected by the standard deviation values. The average size of the IN storms, as indicated by RMW$_{2km}$, is smaller than is the case for SS storms, though that difference is not statistically significant at the 95% confidence level. The SHIPS-derived 850–200-hPa vertical shear magnitude is nearly the same for both databases, though the shallow shear (i.e., the 850–500-hPa vertical shear) does show that the IN storms have a weaker shear than the SS storms, significant at the 95% confidence level. The difference in the direction of the SHIPS-derived 850–200-hPa vertical shear vector and the storm motion vector is $\sim 75°$ for the IN storms, whereas it is $\sim 110°$ for the SS storms. This difference is also significant at the 95% confidence level, and it indicates that storms whose motion vectors are more closely aligned with the shear vector are more likely to intensify than those whose motion vectors are less closely aligned with the shear vector. Finally, the SHIPS-defined sea surface temperature is nearly the same for IN and SS storms (29.5° versus 29.2°C, respectively), though, with such small standard deviations, that difference is statistically significant. However, it is not considered an important signal that could explain the differences in the IN and SS databases, since 29.2°C is still sufficiently warm to allow deep convection and storm intensification.

b. Symmetric structure

The azimuthally averaged kinematic structure of composite-mean IN and SS cases are shown in Figs. 3–6. These structures are plotted with respect to height and
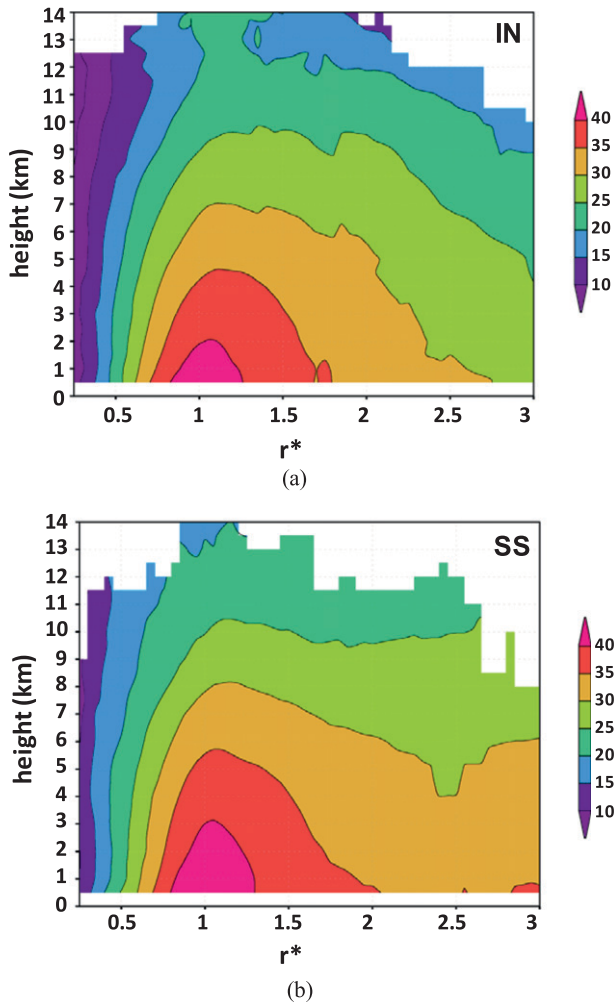
FIG. 3. Normalized radius–height plots of composite-mean axisymmetric tangential wind (color shaded, m s^{-1}) for the (a) IN and (b) SS TC composites. A minimum of eight IOPs at any given location in radius–height space is required to plot the field.

FIG. 4. As in Fig. 3, but for axisymmetric vertical vorticity ($\times 10^{-4}$ s^{-1}).

normalized radius r^*. Figure 3 shows the comparison of composite-mean axisymmetric tangential wind for IN and SS storms. The structure of the primary circulation around the eyewall shows very little difference between the IN and SS cases. The vertical decay of tangential wind shows that the scaled tangential wind at 8 km for IN cases is slightly less than the scaled wind for SS cases, indicating a stronger decay between 2 and 8 km for IN compared with SS cases. This result is in contrast to that shown by Nolan et al. (2007), who showed that a deeper, more barotropic vortex intensified more in their linear model study, though their result focused on TCs of tropical storm strength. The difference between the IN and SS cases is not significant at the 90% confidence level (see Table 3 for a summary of these comparisons), however, so a definitive statement on the agreement (or disagreement) of these results with those of Nolan et al.
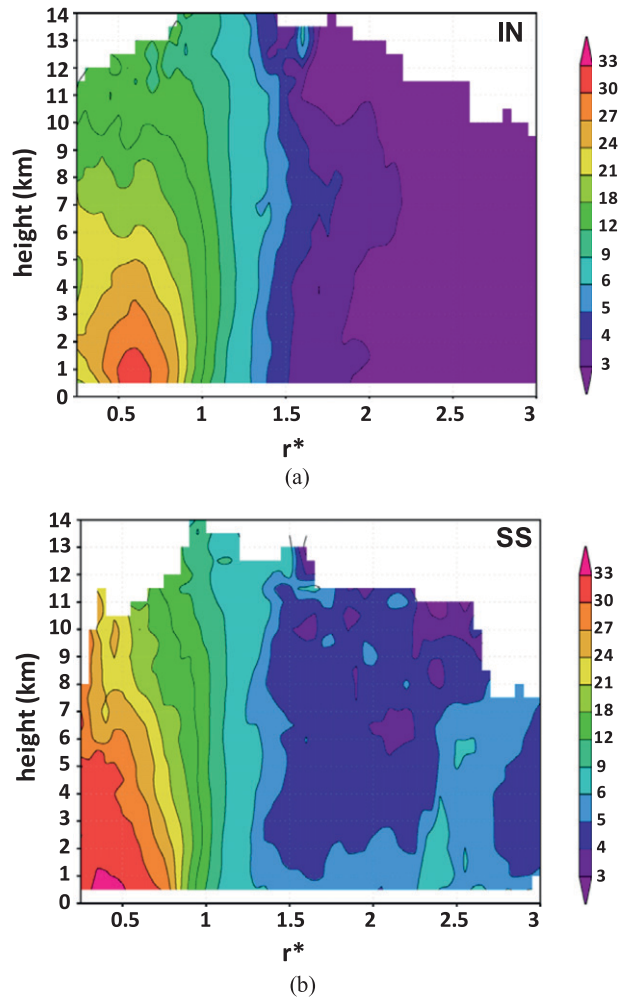
(2007) cannot be made. There is, however, a noteworthy difference at the outer radii (i.e., between $r^* = 2$–3; termed the outer core here). The SS cases have a stronger outer-core tangential wind field, with evidence of a secondary wind maximum outside $r^* = 2.5$, perhaps related to rainband activity or the presence of secondary eyewalls. This contrasts with the outer-core wind field in the IN cases, which show a monotonic decrease with increasing radius. When scaled by the tangential wind at the RMW, the value of the outer-core wind field for SS storms is greater than the value of the wind field for IN cases, significant at the 95% confidence level (cf. Table 3). Such a radial profile for SS cases is indicative of higher inertial stability.

The axisymmetric vertical vorticity is shown in Fig. 4. The basic patterns for both the IN and SS cases show vorticity maximized inside the RMW below 5-km altitude and rapidly decreasing radially outward from the
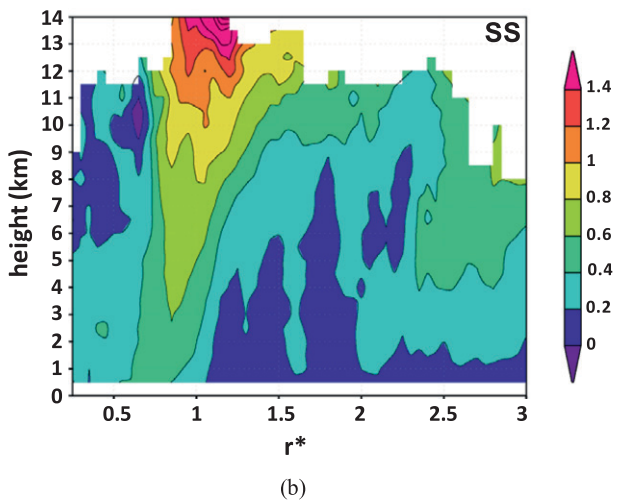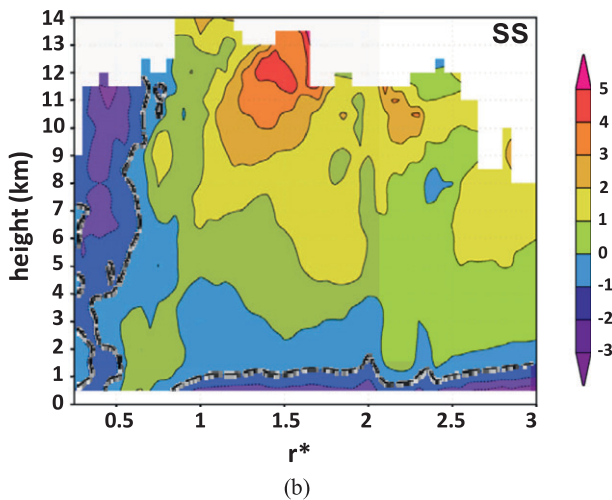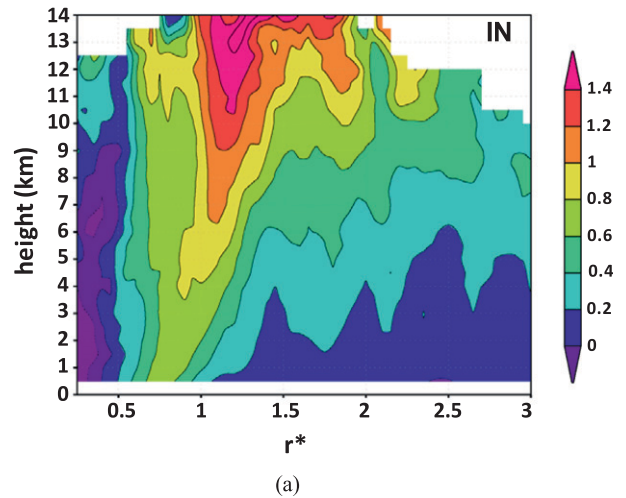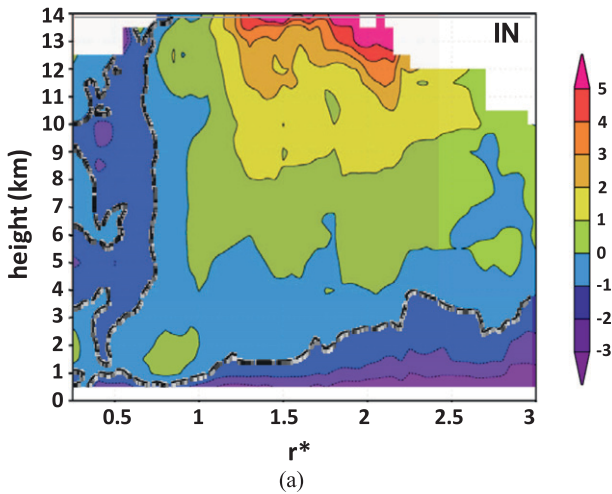
FIG. 5. As in Fig. 3, but for axisymmetric radial wind (m s^{-1}). Boldface dashed line denotes contour value of -1 m s^{-1}.

FIG. 6. As in Fig. 3, but for axisymmetric vertical velocity (m s^{-1}).

RMW. For the IN cases, though, a clear ringlike structure is evident below 4-km altitude and between $r* = 0.3$ and 0.6. This contrasts with the SS cases, which show more of a monopolar structure inside the RMW. The ratio of axisymmetric vorticity at $r* = 0.3$ to that at $r* = 0.6$ (i.e., the "scaled inner eyewall vorticity"; cf. Table 3) provides a measure of the shape of the inner eyewall vorticity profile, since values of this scaled vorticity that are <1 are indicative of a ring of vorticity whereas values that are >1 are indicative of a monopole. Significant at the 95% confidence level, these features are consistent with the "U shaped" and "V shaped" wind profiles found in flight-level composites of intensifying and post-intensifying TCs in Kossin and Eastin (2001). Within the outer core, significant differences in the vorticity distribution are noted as well. The SS cases have much higher vorticities than do the IN cases, including a secondary maximum at $r* = 2.5$. Also indicative of greater

outer-core inertial stability for SS cases (similar to the tangential wind comparisons in Fig. 3), this difference is significant at the 99% confidence level.

Figure 5 shows a comparison of axisymmetric radial flow for the IN and SS cases. As highlighted by Ooyama (1982), vortex intensification is ultimately tied to increasing net vertical mass flux within the inner core driven by an amplifying secondary circulation pattern, composed of a deep-layer radial inflow and upward motion in the ascending branch of the circulation. Both composites here show many of these features: symmetric inflow maximized in the lowest 1-km altitude, the depth of which increases with increasing distance from the RMW; a broad layer of weaker inflow above that; an area of outflow just inside the RMW and above the inflow at about 2-km altitude; and the return flow of the secondary circulation above 6-km altitude, reaching a peak in the upper troposphere. These structures are

TABLE 3. Summary statistics comparing various inner-core parameters for IN and SS tropical cyclones. Statistics shown include mean, standard deviation, and *t* statistic. Maximum significance level exceeded using one-sided Student's *t* test shown. Values that are boldfaced denote differences in the mean that are significant at the ≥95% confidence level. Details on the calculation methodology for each parameter are given in the appendix.

Parameter	IN		SS		*t* statistic	Significance level (%)
	Mean	Std dev	Mean	Std dev		
Scaled outer-core tangential wind (dimensionless)	**0.733**	0.084	**0.809**	0.127	−1.773	95
Scaled vertical profile of eyewall tangential wind (dimensionless)	0.697	0.076	0.730	0.070	−1.195	<90
Scaled inner-eyewall vorticity (dimensionless)	**0.816**	0.399	**1.037**	0.207	−1.839	95
Scaled outer-core vorticity (dimensionless)	**0.143**	0.054	**0.396**	0.180	−4.849	99
Inflow strength (m s^{-1})	−2.925	1.889	−1.589	3.064	−1.389	90
Inflow depth (km)	**4.300**	2.444	**1.800**	1.366	2.485	95
Eyewall vertical velocity (m s^{-1})	**0.844**	0.344	**0.567**	0.469	1.781	95
Radial location of convective bursts (dimensionless)	**0.907**	0.334	**1.048**	0.352	−6.238	99

consistent with those seen in recent observational composite studies of mature TCs (e.g., Zhang et al. 2011; Rogers et al. 2012) and have been well documented in past modeling studies. There are some differences in the structure of the axisymmetric radial flow between the IN and SS composites, however. The IN cases show stronger inflow near the surface, though this difference is only significant at 90%. Outside the RMW ($r* = 1.5–2.5$), the depth of the inflow, defined here as the location of the −1 m s^{-1} contour, is significantly larger (95% significance) for the IN cases. Kepert (2001) showed that boundary layer depth is inversely proportional to inertial stability. Figure 4 shows that the axisymmetric vorticity, which is related to inertial stability, is lower in these outer radial bands for IN cases than for SS cases (cf. Fig. 4). This relationship is therefore consistent with that described in Kepert (2001).

Montgomery and Smith (2012) and Smith et al. (2009) discuss two modes of radial inflow and describe how they each lead to changes in the TC structure and intensity: deep, relatively weak inflow converges absolute angular momentum above the boundary layer, where it is conserved, resulting in a broadening of the outer circulation, while the strong inflow in the lowest 1 km also converges angular momentum, though this quantity is not conserved and the convergence produces the maximum tangential winds in the boundary layer. As mentioned above, the composites show deeper inflow (extending up to 4–5 km) for IN cases, which would suggest that those cases would see a broadening of their circulations over time compared with the SS cases. The size parameter was not a focus of this investigation, however, so this question cannot be answered here. Further, IN cases show stronger inflow in the lowest 1 km, which would suggest a stronger convergence of absolute angular momentum and a larger spinup of tangential winds in the boundary layer. However, since the radar analyses only extend down to 500 m, they are missing the altitudes closest to the surface where radial inflow is typically the strongest (Lorsolo et al. 2010; Zhang et al. 2011; Rogers et al. 2012), so a stronger signal may be masked by the limitations in the dataset analyzed here. A more definitive testing of the hypotheses discussed in Montgomery and Smith (2012) and Smith et al. (2009) awaits additional datasets that may be better able to resolve the flow in the lowest 1 km.

The axisymmetric vertical velocity fields are shown in Fig. 6. Rising motion, associated with the ascending branch of the secondary circulation and manifested in the axisymmetric component of vertical velocity, is apparent inside the RMW. This rising motion slopes radially outward with height for both IN and SS cases. Outside the RMW there are weak updrafts and an indication of stronger upward motion for the SS cases. This stronger upward motion, coupled with the stronger outer-core tangential wind and higher vorticity (cf. Figs. 3 and 4), likely indicates the presence of more rainband and secondary eyewall activity for the SS cases (Rozoff et al. 2012). Eyewall upward motion is stronger in the middle and upper troposphere for the IN cases. This difference is significant at the 95% confidence level. Downward motion is also evident inside $r* = 0.5$ for IN cases between 0.5- and 10-km altitude, compared with weak upward motion for SS cases.

c. Asymmetric structure

Examples of the asymmetric structure of IN and SS cases are shown in Figs. 7–11. Figure 7 shows the composite mean displacement of the vortex center between 2- and 7-km altitude for each of the datasets. For both IN and SS cases the vortex on average tilts toward the downshear side of the storm, with an orientation between 30° and 60° to the left of the local shear vector. This is broadly consistent with that shown in observational- and modeling-based studies of TCs in shear (e.g., Reasor et al. 2004, 2013; Braun and Wu 2007; Davis et al. 2008; Riemer
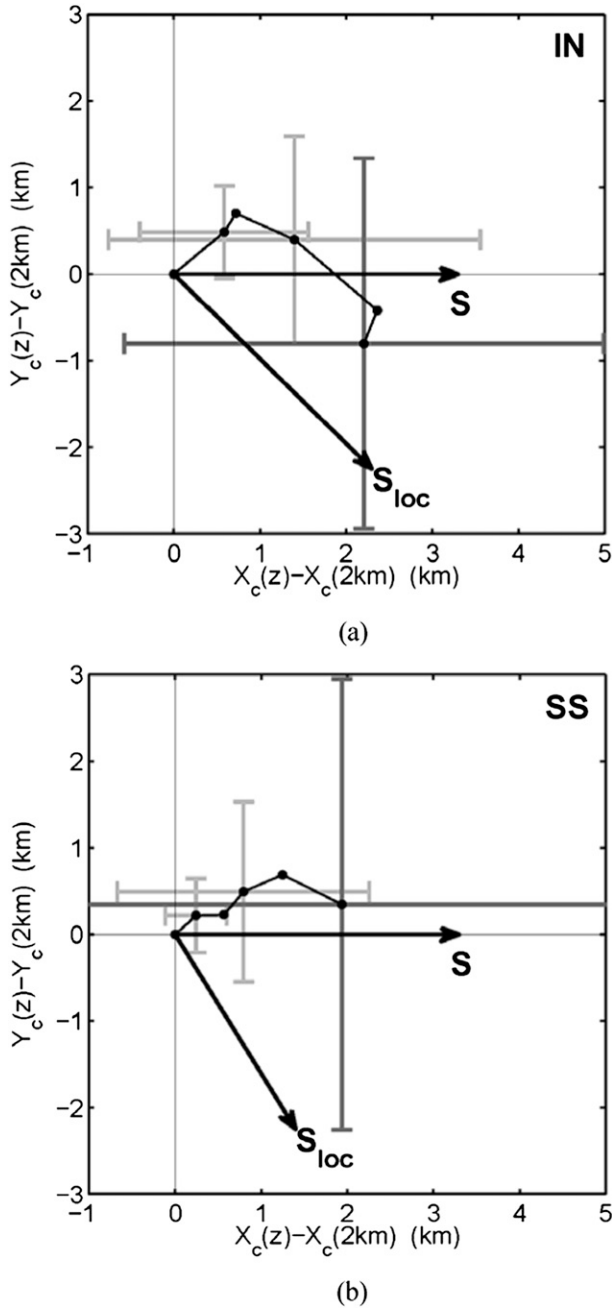
FIG. 7. Shear-relative composite of vortex center (X_c, Y_c) tilt at 1-km intervals from 2 to 7 km for (a) IN and (b) SS cases. The tilt structure for each contributing case is referenced to the center at 2 km. The 95% confidence intervals (bars in x and y) are shown at 3, 5, and 7 km. The radar-estimated 2–9-km local shear is indicated by S_{loc} (not to scale).

FIG. 8. Composite-mean reflectivity (color shaded, dBZ) at 2 km and vertical velocity (contours, m s^{-1}) at 5 km for (a) IN and (b) SS TC composites. Fields are plotted relative to the 850–200-hPa vertical shear vector obtained from SHIPS (boldface arrows pointing to the right).

et al. 2010). The magnitude of the tilt for both datasets is ~(2–3 km, and there is no statistically significant difference in the tilt magnitude. While similar magnitudes of tilt were seen in the Doppler analysis of rapidly intensifying
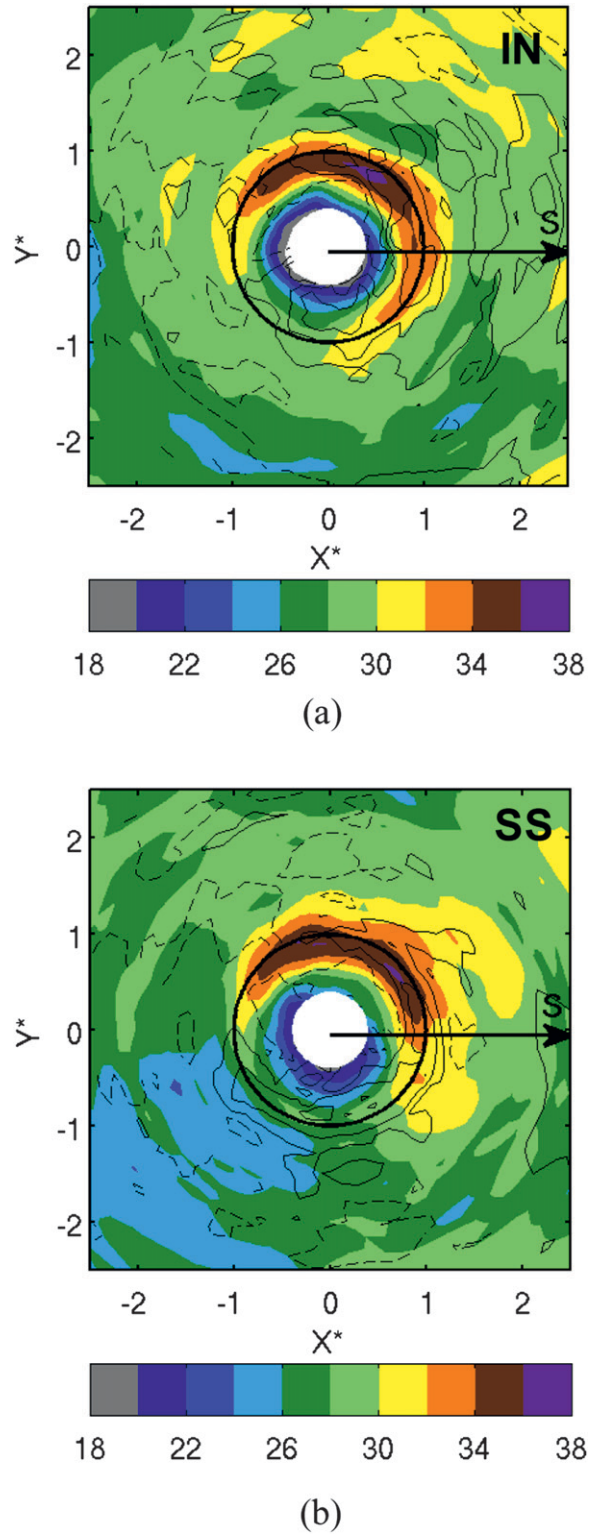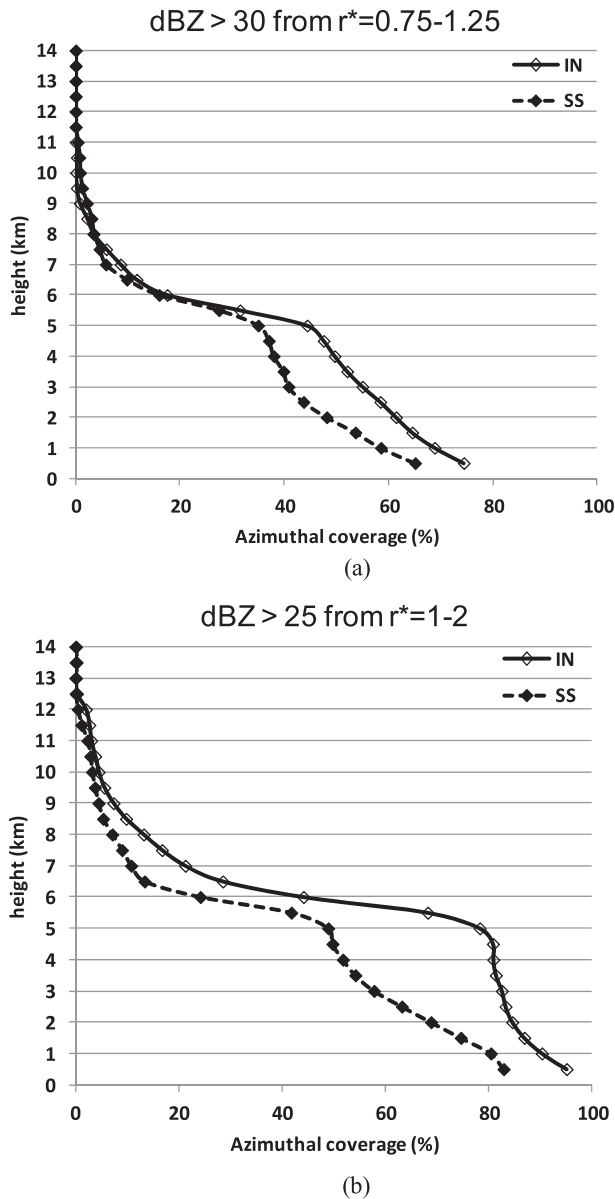
FIG. 9. (a) Vertical profiles of the azimuthal coverage of reflectivity (%) exceeding 30-dBZ threshold for IN (solid line with open diamonds) and SS (dashed line with filled diamonds) cases in the $r^* = 0.75$–1.25 annulus. (b) As in (a), but for cases exceeding the 25-dBZ threshold in the $r^* = 1$–2 annulus.

a peak beginning upwind of the reflectivity maximum and wrapping around to the left of the shear azimuth. A minimum of reflectivity and negative vertical velocity is seen on the upshear side of the storm. While the basic azimuthal phase and amplitude of the reflectivity and vertical velocity asymmetry are similar between both datasets, there is a difference in the azimuthal coverage of reflectivity for IN cases; namely, there is in general greater coverage of reflectivity both within and outside the eyewall for IN cases compared with SS cases.

Figure 9 shows vertical profiles of the azimuthal coverage of reflectivity exceeding a threshold of 30 dBZ within the eyewall ($r^* = 0.75$–1.25) and exceeding 25 dBZ in an annulus outside the eyewall ($r^* = 1$–2). For both metrics the IN cases showed a greater azimuthal coverage than did the SS cases, though this difference is larger outside the eyewall. This relationship between azimuthal coverage of precipitation and TC intensification was also noted in ring structures that are associated with TC intensification based on analyses of 37-GHz microwave images (Kieper and Jiang 2012) and in the symmetry of inner-core convection discussed by Kaplan et al. (2010). This difference in azimuthal coverage may be due to the differences in the magnitude of vertical shear. In particular, the value of 850–500-hPa SHIPS-derived shear is higher for SS cases compared with IN cases (cf. Table 2). The stronger shear in SS cases can lead to stronger asymmetries in the precipitation field, which would be manifested as a smaller azimuthal coverage of precipitation. Also note that the difference in azimuthal coverage is maximized below the freezing level (i.e., ~5 km), whereas above the freezing level there is little to distinguish between the IN and SS cases. One possible explanation why there is less difference above the freezing level is related to the different average fall speeds in these layers. While vigorous updrafts can transport frozen rain and graupel above the freezing level, much of the precipitating area above the freezing level consists of low-density ice and aggregates (Houze et al. 1992; Black et al. 1996). The fall speeds of these particles are comparatively slow. Because of these slow fall speeds, these hydrometeors can remain aloft for extended periods of time, where they can be advected for significant distances azimuthally by the primary circulation (Marks and Houze 1987; Houze et al. 1992). As a result, any differences in the azimuthal coverage of reflectivity could be smeared out through this "mixmaster" effect (Marks and Houze 1987; Rogers et al. 2009) at these altitudes. By contrast, below the freezing level the raindrops fall at a much faster fall speed, so any differences in the azimuthal coverage of the production of precipitation are more likely to be retained.

Hurricane Guillermo (1997; Reasor et al. 2013), tilt magnitude does not appear to be a feature that distinguishes IN from SS TCs.

Figure 8 shows the 2-km reflectivity and 5-km vertical velocity fields for IN and SS cases, plotted relative to the 850–200-hPa shear vector. Consistent with many previous studies (e.g., Black et al. 2002; Reasor and Eastin 2012; Reasor et al. 2000, 2009, 2013), the peak in eyewall reflectivity is located in the downshear-left quadrant for both IN and SS cases. The vertical velocity also shows
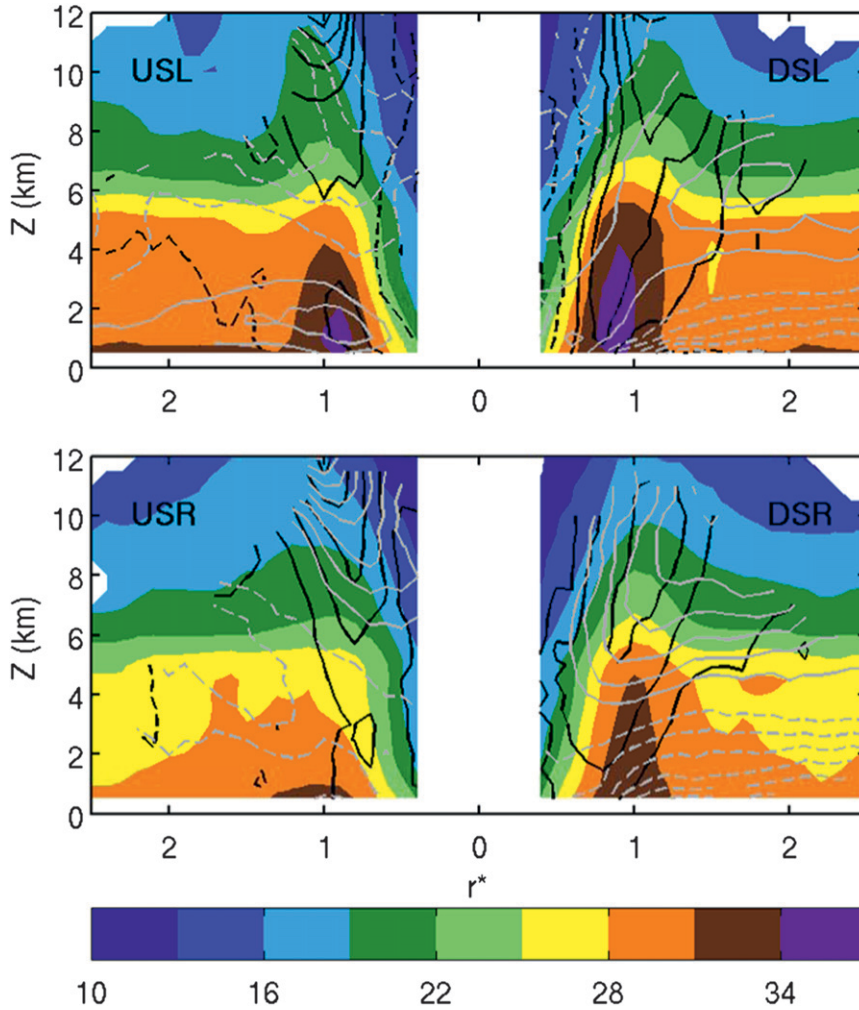
FIG. 10. Quadrant-average cross sections of shear-relative composite reflectivity (color shaded, dBZ), vertical velocity (black contours, m s^{-1}), and radial velocity (gray contours, m s^{-1}) for IN cases. The quadrants are arranged such that the shear vector points to the right of the page. Negative values of vertical velocity are bounded by the dashed black contour, and positive values are contoured from 0.5 m s^{-1} at an interval of 0.5 m s^{-1}. The contour interval for radial inflow (dashed gray) and outflow (solid gray) is 1 m s^{-1} (0 contour omitted). The radial coordinate r^* is scaled by RMW$_{2km}$.

Vertical cross sections of the azimuthal variation in the kinematic and precipitation fields are shown in Figs. 10 and 11. In these plots, fields of radial flow, vertical velocity, and reflectivity are averaged within quadrants oriented relative to the 850–200-hPa vertical shear vector, similar to the analysis shown in Reasor et al. (2013). The quadrant analyses for IN cases (Fig. 10) show the impact of the vertical shear on the radial flow and reflectivity structure. A deep layer of inflow is seen in the downshear-right (DSR) and downshear-left (DSL) quadrants, while outflow is apparent in the low levels in the upshear-left (USL) quadrant. A strong upper-level return flow is seen in the DSR and DSL quadrants, while

upper-level inflow is seen in the USL quadrant. The vertical velocity field shows upward motion in all quadrants in the eyewall, though this upward motion is strongest, and extends to the lowest levels, in the DSR and DSL quadrants. In the DSR and DSL quadrants the upward motion extends out to larger radii outside the eyewall, indicative of a larger presence of stratiform precipitation at these larger radii. The reflectivity field shows that the highest values of eyewall reflectivity are located within the DSL quadrant and continue into the USL quadrant, while a minimum is seen in the upshear-right (USR) quadrant. This pattern is consistent with the plan-view plot shown in Fig. 8. For the SS cases (Fig. 11),
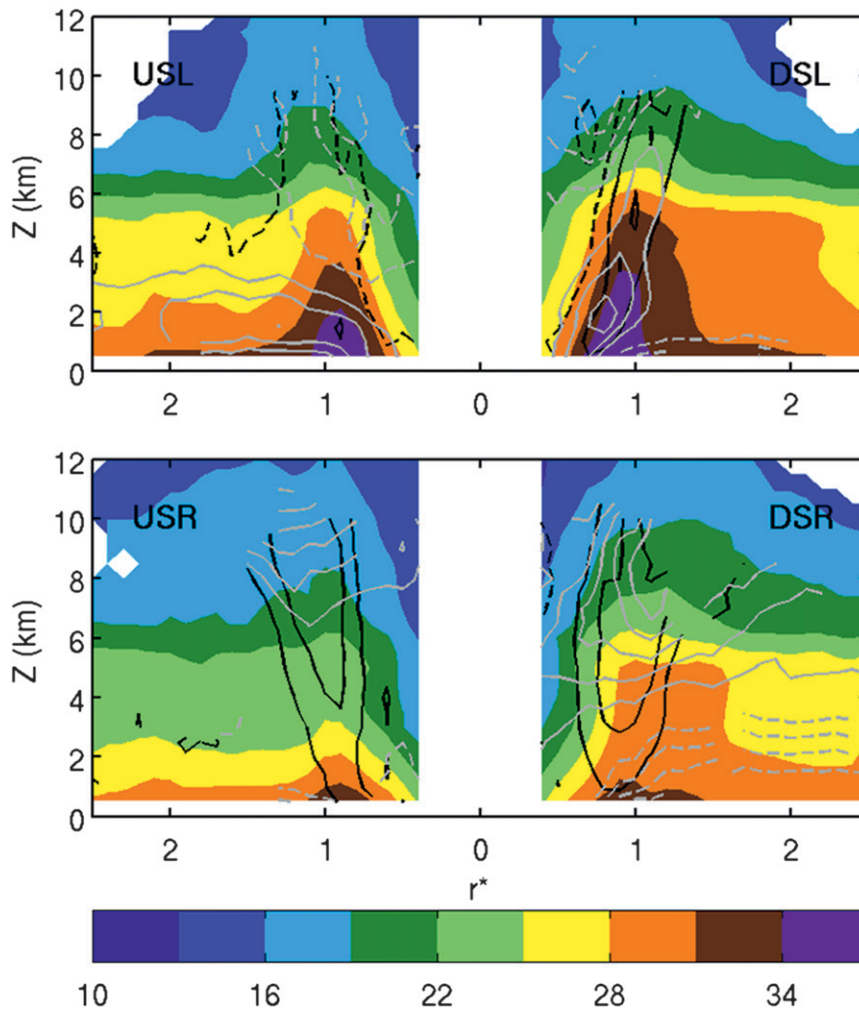
FIG. 11. As in Fig. 10, but for SS cases.

the pattern shows many similarities to the IN cases. There are some noteworthy differences, however. In particular, the magnitude of the secondary circulation in the DSL quadrant is weaker for SS cases. This is seen in the shallower and weaker area of low-level inflow, and the absence of upper-level return flow, in the DSL quadrant. Additionally, there is an absence of upper-level eyewall upward motion in the USL quadrant. This may help to explain the reduction in the azimuthal coverage of precipitation in the USR quadrant for SS cases shown in Figs. 8 and 9.

4. Convective structure

Characteristics of the convective-scale structure for IN and SS cases are now examined. Such a comparison is primarily performed by examining statistical properties of the vertical velocity field within and near the eyewall,

which for this study is defined as normalized radii ranging between $r* = 0.75$ and 1.25. As mentioned above, for the analyses shown here individual radial passes are used to construct the composites rather than IOPs, which tend to smooth much of the smaller spatial and temporal-scale fields associated with convective-scale features.

Figure 12 compares characteristics of the vertical velocity distribution within the eyewall for IN and SS cases. Figure 12a shows the number of $2 \times 2 \, km^2$ points used to calculate the statistics shown in subsequent figures. The number of points for both cases increases from 20 000 at 0.5-km altitude to a peak of ~35 000 at 2-km altitude; then decreases steadily to below 5000 above 14-km altitude. Even though there are fewer radial passes for the IN versus the SS cases (40 versus 53; cf. Table 1), there are more points within the eyewall for IN cases. However, both samples have a large number of
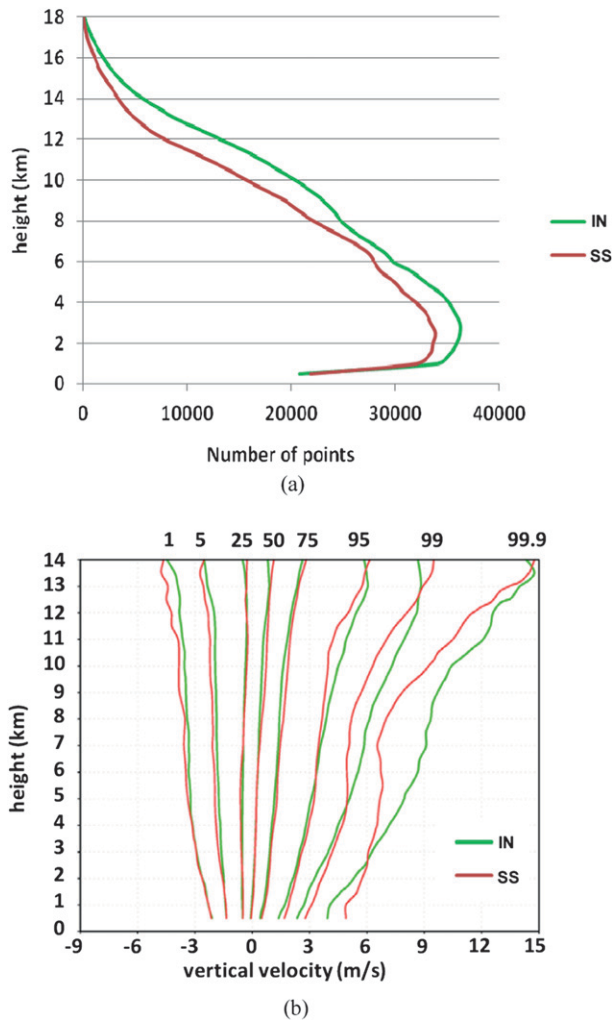
FIG. 12. (a) Vertical profile of the number of points sampled in the eyewall region (defined as r^* values $0.75 – 1.25$) from individual radar passes used to calculate statistics of vertical velocity for IN (green) and SS (red) TCs. (b) Vertical profile of select percentiles (1, 5, 25, 50, 75, 95, 99, and 99.9th percentiles) of the cumulative distributions of eyewall vertical velocity from individual radar passes in IN (green) and SS (red) TCs.

points, so confidence in the robustness of the comparisons is high for a significant range of altitudes. To ensure an adequate number of points, only altitudes below 14 km are considered here.

Differences in the distribution of eyewall vertical velocity for IN and SS cases are shown in Fig. 12b. The vertical profile of the cumulative distribution function of eyewall vertical velocity for each dataset is shown, with select percentiles (i.e., the 1st, 5th, 25th, 50th, 75th, 95th, 99th, and 99.9th percentiles) highlighting similarities and differences in different portions of the distributions. The middle portion of the distributions (i.e., the 25th–75th percentiles) compares the weak-to-moderate range

of the vertical velocity spectrum between the datasets, while the ends of the distributions (i.e., the ≤5th and ≥95th percentiles) compare the extreme ends of the spectrum (i.e., strong downdrafts and updrafts, respectively). For both IN and SS cases, the median of the distribution (i.e., the 50th percentile) shows very weak upward motion throughout the depth of the troposphere, with minimal difference between the datasets. The remainder of the middle portion of the distribution spans weak vertical velocity, with the 25th percentile $\sim-0.2\,\mathrm{m\,s}^{-1}$ and the 75th percentile $\sim0.5\,\mathrm{m\,s}^{-1}$. It is clear that, even in the eyewall, the majority of vertical velocities are composed of weak drafts, consistent with past observational studies using flight-level and airborne Doppler data (e.g., Jorgensen 1984; Jorgensen et al. 1985; Black et al. 1996; Rogers et al. 2007, 2012). There is little difference in the magnitudes of the 25th–75th percentiles between the IN and SS cases. There is also little difference in the magnitudes of the low end of the distribution (i.e., the strong to moderate downdrafts). It is not until the high end of the distribution, representing the most vigorous updrafts, that noteworthy differences between IN and SS are seen. For example, the magnitude of the 99th percentile at 7-km altitude is $6\,\mathrm{m\,s}^{-1}$ for IN and $5\,\mathrm{m\,s}^{-1}$ for SS cases, while the magnitude of the 99.9th percentile at 7-km altitude is $9\,\mathrm{m\,s}^{-1}$ for IN and $6\,\mathrm{m\,s}^{-1}$ for SS cases. While this is a small fraction of the total number of points, the difference is large. This result indicates that, within the eyewall, there is little difference in the magnitude of the bulk of the vertical velocity distribution, as well as strong to moderate downdrafts, for IN and SS cases. Rather, most of the difference in the eyewall vertical velocity distribution between the IN and SS cases is contained at the top of the distribution, representing the strongest updrafts, and it is most clearly seen above 4–5 km (i.e., above the freezing level).

How these differences are manifested in eyewall vertical mass flux profiles is shown in Fig. 13. Similar to Hence and Houze (2008), the air density used in the vertical mass flux calculation is from the Jordan (1958) standard tropical Atlantic atmospheric profile for the hurricane season. Figure 13a shows the vertical profile of positive, negative, and net vertical mass flux for the eyewall region of IN cases, normalized by the maximum positive vertical mass flux value. Updraft mass flux is peaked at ~3.5-km altitude, though the value of this peak extends over the 3–4.5-km layer. The updraft mass flux decreases to 74% of its maximum by 11 km. Downdraft mass flux peaks below ~2-km altitude, with a magnitude $\sim60\%$ of the peak updraft mass flux. The net vertical mass flux, representing the difference between the updraft and downdraft mass fluxes, starts at $\sim25\%$ of the peak updraft mass flux in the lowest 1-km

Peak = 3.35 x 10^6 kg s^{-1}

(a)

(b)

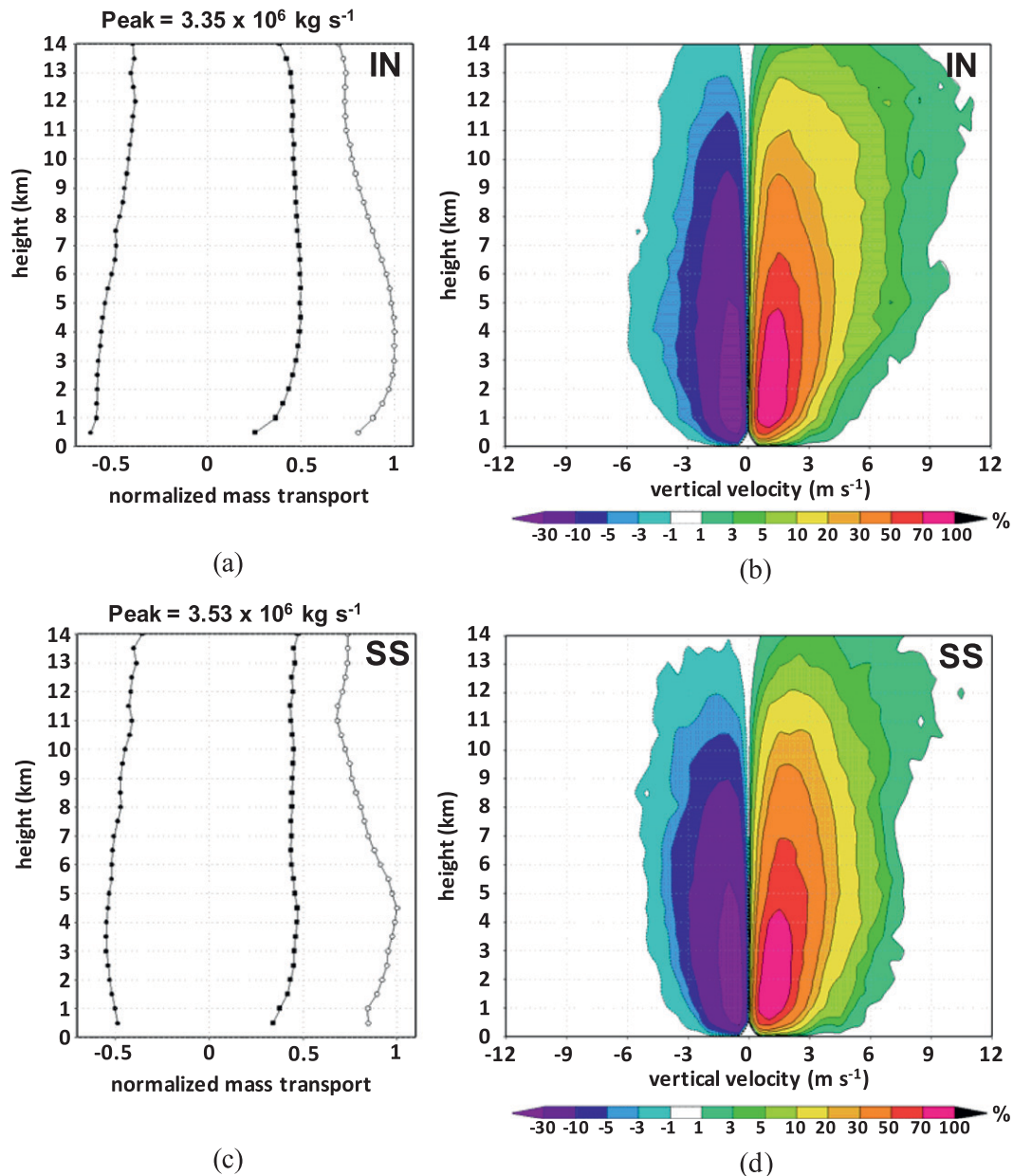Peak = 3.53 x 10^6 kg s^{-1}

(c)

(d)

FIG. 13. (a) Vertical profile of positive (open circle), negative (closed circle), and net (closed box) vertical mass transport in the eyewall region for intensifying TCs normalized to the maximum positive vertical mass transport value (peak value indicated). (b) Vertical mass transport-weighted vertical velocity CFAD (color shaded, %) in the eyewall region for intensifying TCs normalized to the maximum positive vertical mass transport value binned every 0.5 m s^{-1}. (c) As in (a), but for SS TCs, (d) As in (b), but for SS TCs.

layer before increasing to ~50% by 4-km altitude, where it remains until near the top of the profile. The profiles for SS cases (Fig. 13c) show a similar general shape, but there are some differences. In particular, the peak updraft mass flux is at a higher altitude (~4.5 km) and the peak is confined to a narrower layer for SS cases. Additionally, the updraft mass flux decreases with altitude more quickly than the IN cases, decreasing to 68%

of its maximum by 11 km (compared with 74% for IN cases). The downdraft mass flux is generally consistent with the IN cases, with the exception of a weaker magnitude of downdraft mass flux in the lowest 2 km. The net vertical mass flux peaks at ~4-km altitude, similar to the IN cases, but it shows a larger decrease with height compared with the IN cases, most notably between 5- and 10-km altitude. This difference is consistent with

that shown in the axisymmetric vertical velocity (cf. Fig. 6), though the difference is not as pronounced for the mass flux profiles.

Figures 13b,d shows vertical mass-transport-weighted contoured frequency by altitude diagrams (CFADs; Yuter and Houze 1995; Hence and Houze 2008) normalized by the peak positive vertical mass flux value (negative percentages reflect downward mass transport). This shows how eyewall vertical mass transport is accomplished by the various portions of the vertical velocity spectrum. The broad shape of the distribution of the vertical mass flux across vertical velocity values for the IN and SS cases is similar. The bulk of the vertical mass transport is accomplished by the weak up- and downdrafts (1–$2\,m\,s^{-1}$ up, 0.5–$1\,m\,s^{-1}$ down) for both IN and SS cases. This is expected, since they compose the bulk of the vertical velocity spectrum (cf. Fig. 12b; Yuter and Houze 1995; Hence and Houze 2008; Rogers 2010). For IN cases, however, a larger percentage (10%–20% for updraft, 3%–5% for downdraft) of the vertical mass flux is accomplished by weak drafts that extend to a higher altitude than for SS cases. A more notable difference is evident in updraft mass flux from strong drafts ($>5\,m\,s^{-1}$) above 6-km altitude for IN cases. More than 10% of the peak updraft mass flux is accomplished by strong drafts above 6-km altitude for IN cases, compared with 5%–10% from SS cases. When considering more extreme ends of the updraft spectrum, the difference is even more pronounced, with 3%–5% occurring from drafts $>7\,m\,s^{-1}$ for IN at 8-km altitude and $\sim$1% occurring from the same range of drafts for SS cases. The results shown in Figs. 12 and 13 indicate that, from the standpoint of eyewall vertical velocity and vertical mass flux statistics, there is little to distinguish IN from SS cases in terms of the bulk of the distributions. Rather, the primary difference lies in the high end of the distributions, where IN cases have a higher percentage of the most vigorous updrafts, and these updrafts transport a larger percentage of mass flux in the vertical.

To pursue this issue further, the vertical velocity distribution was examined for each radial pass to determine the location of convective bursts. Bursts in this context are defined as the top 1% of the vertical velocity distribution at 8-km altitude for the combined IN and SS datasets. Using this definition, the burst threshold is set at $5.5\,m\,s^{-1}$. Figure 14 shows the locations of bursts in normalized Cartesian coordinates from all radial passes for the IN and SS cases. Each X denotes a point in the radar analysis that exceeds the threshold defining a convective burst. The locations of the bursts are rotated to be plotted relative to the 850–200-hPa SHIPS-derived shear vector, which points to the right in this figure for both cases. Both IN and SS cases show that the
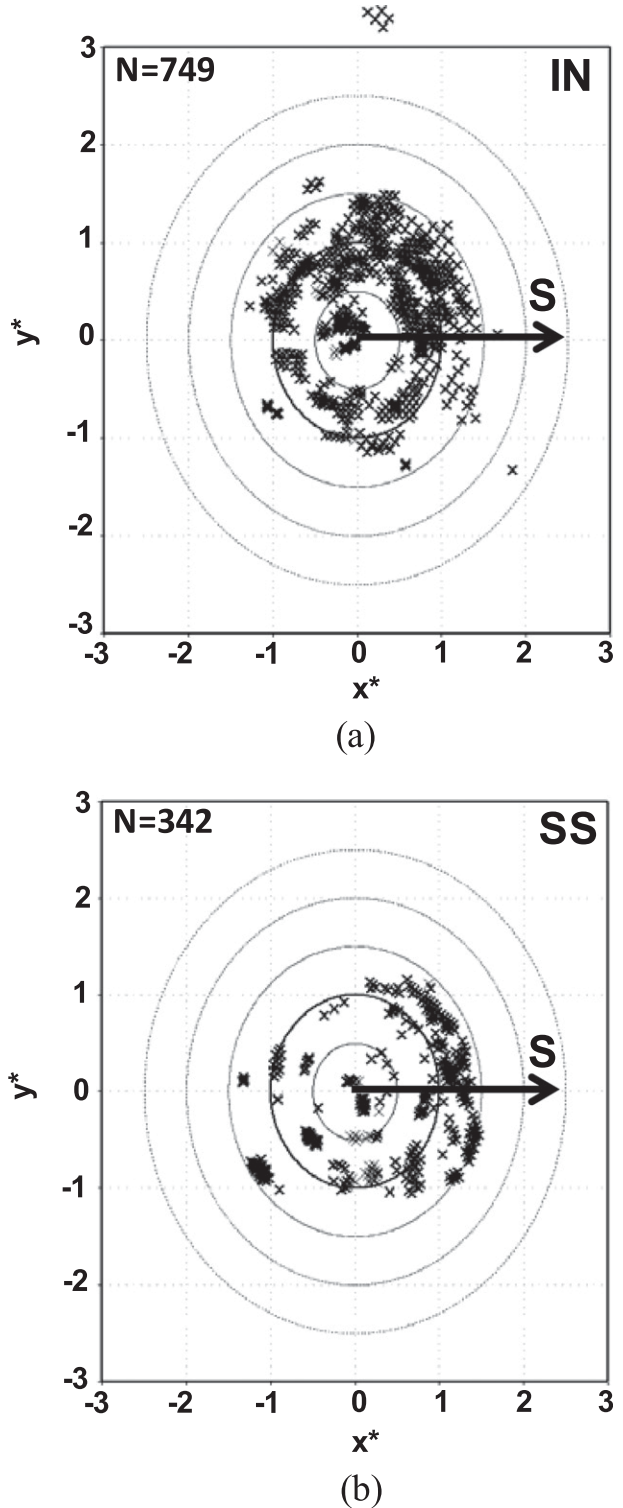

(a)

(b)

FIG. 14. Location of convective burst points (definition provided in text) for (a) IN and (b) SS TCs. Burst locations are plotted in normalized radial coordinates ($x^* = x$/RMW, $y^* = y$/RMW) relative to the 850–200-hPa vertical shear vector obtained from SHIPS (boldface arrows pointing to the right).

majority of the bursts are located in the downshear and downshear-left regions, consistent with past observational and modeling studies (e.g., Reasor et al. 2009; Braun and Wu 2007; Braun et al. 2006; Rogers et al. 2003; Black et al. 2002). The primary difference that is clear from this comparison is the higher number of burst points found for IN cases compared to SS cases (749 versus 342). The number of burst points for IN cases is more than twice the number for the SS cases, but this higher number for the IN cases cannot be simply explained by the larger number of points, which is higher by only about 20% for the IN cases at 8-km altitude (cf. Fig. 12a). Burst points appear to be preferentially located in the downshear-left quadrant for IN cases, whereas for SS cases the burst points are more evenly distributed in the downshear-left and downshear-right quadrants. The higher number of burst points in the downshear-left quadrant for IN cases is consistent with the quadrant-averaged structures shown in Figs. 10 and 11. Specifically, the deeper and stronger low-level inflow layer in the downshear-left quadrant for IN cases supports stronger eyewall convection, some of which can be classified as convective bursts. Furthermore, as the updrafts within these bursts ascend and are advected around the storm, they provide a greater contribution to the quadrant-averaged vertical velocity field downwind. As a result, the quadrant-averaged eyewall vertical velocity shows an upward motion peak in the upshear-left quadrant for the IN cases.

Another difference that can be detected upon closer inspection is a larger proportion of burst points inside the RMW ($r^* = 1$) for IN cases. This is more clearly shown in Fig. 15, which shows the radial distribution of convective burst points for both cases overlain on the axisymmetric vertical vorticity (adapted from Fig. 4). The IN cases show a peak in the distribution of burst points between $r^* = 0.75$ and 1, while the SS cases show the peak is between $r^* = 1.25$ and 1.5. With a confidence level of 99% (Table 3), the difference between the radial location of bursts for the IN and SS cases is the most significant of the parameters studied here. The peak of the distribution for burst points for the IN cases occurs where the composite mean axisymmetric vorticity is $\sim 20 \times 10^{-4}\,\mathrm{s}^{-1}$, whereas the peak for the SS cases occurs where the vorticity is $\sim 5 \times 10^{-4}\,\mathrm{s}^{-1}$. This is an important difference because the strongest diabatic heating from these vigorous updrafts, preferentially located in the high-vorticity region inside the RMW for the IN cases, is thought to have a much larger impact on TC intensification compared with heating outside the RMW (e.g., Vigh and Schubert 2009; Pendergrass and Willoughby 2009). The relationship between the radial locations of convective bursts and TC intensification has
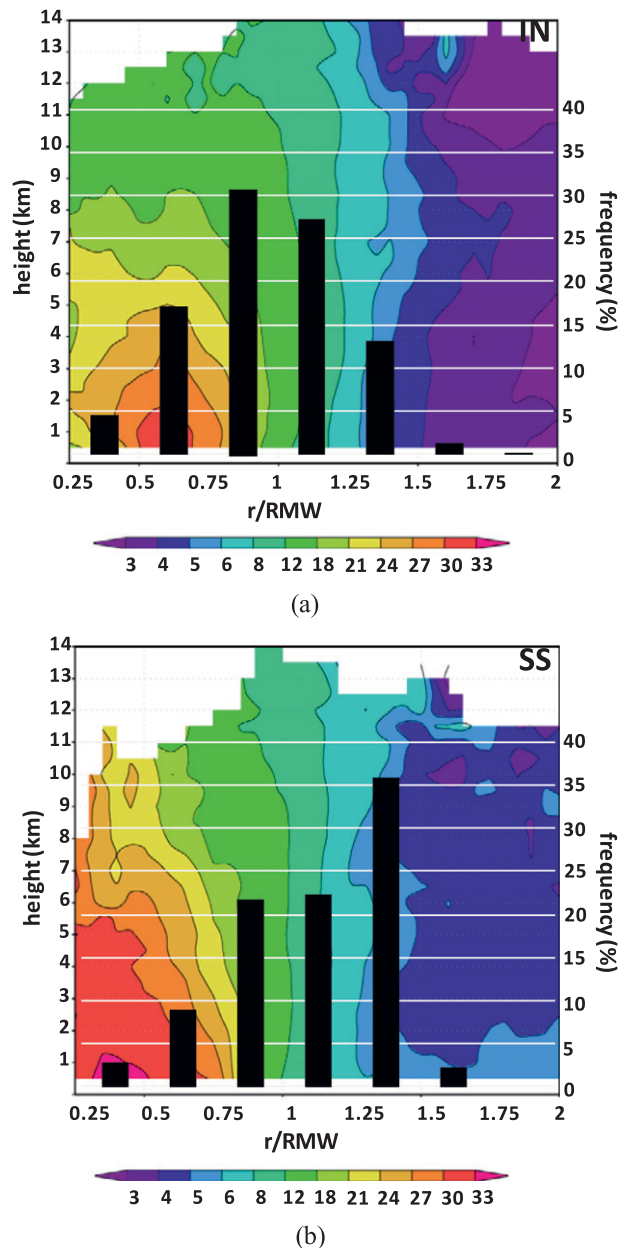

(a)

(b)

FIG. 15. Frequency of convective burst points as a function of normalized radial location (bar chart, %) overlain on normalized radius–height plot of composite-mean axisymmetric vertical vorticity (color shaded, $\times 10^{-4}\,\mathrm{s}^{-1}$, adapted from Fig. 4) for the (a) IN and (b) SS TC composites.

also been shown in modeling studies (Rogers 2010; Zhang and Chen 2012; Chen and Zhang 2013).

5. Summary and concluding remarks

An examination of the differences in the inner-core structure of intensifying and steady-state TCs shows several statistically significant differences. Figure 16
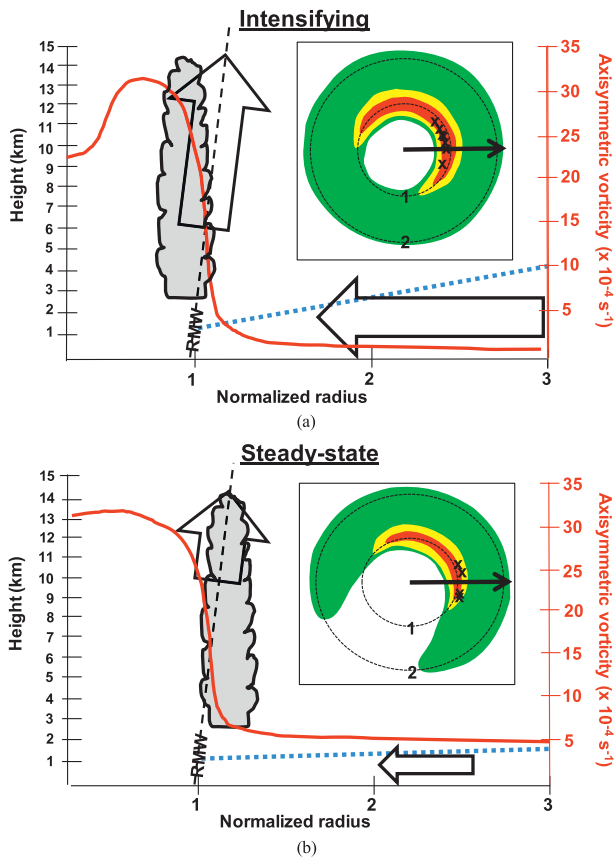
FIG. 16. Summary schematic of the key differences in the inner-core structure of (a) IN and (b) SS tropical cyclones. Black dashed line denotes radius of maximum wind, thick red line denotes radial profile of axisymmetric vertical vorticity ($\times 10^{-4}\,\mathrm{s}^{-1}$) at 2-km altitude, and thick arrows denote axisymmetric radial and vertical wind. Blue dotted line denotes inflow layer defined by axisymmetric radial flow. Gray scalloped area denotes predominant radius of convective bursts. Insets show plan-view depiction of reflectivity at 2-km altitude [shaded, red (green) denotes high (low) reflectivity] and typical location of convective bursts ($\times$ marks). Both reflectivity and convective bursts are rotated relative to 850–200-hPa shear vector (black arrow pointing to right in inset).

provides a schematic summarizing the key differences. In terms of the axisymmetric structure, intensifying TCs have a ringlike vorticity structure inside the RMW and lower vorticity in the outer core (and as a result a lower inertial stability in the outer core) compared with steady-state TCs. Intensifying TCs also have a deeper, stronger inflow layer and stronger axisymmetric eyewall upward motion. There is little difference in the tilt of the vortex between 2 and 7 km, and both intensifying and steady-state TCs show an eyewall precipitation and updraft asymmetry whose maxima are located in the downshear and downshear-left regions. The azimuthal coverage of eyewall and outer-core precipitation, however, is greater for intensifying TCs (inset in Fig. 16).

There is little difference in the distribution of downdrafts and weak to moderate updrafts in the eyewall. The primary difference is seen at the high end of the vertical velocity spectrum, where intensifying TCs appear to have a higher proportion of convective bursts. These bursts accomplish more vertical mass flux, but they compose such a small portion of the total vertical velocity distribution that there is little difference in the shape of the net mass flux profile between the two cases—only a slightly smaller reduction in updraft (and net) mass flux above the freezing level for intensifying TCs. One key difference, though, is that the radial location of convective bursts for intensifying TCs is preferentially located inside the RMW, where the axisymmetric vorticity is generally higher, whereas for steady-state TCs the bursts are located outside the RMW, where the vorticity is lower.

The difference in the outer-core vorticity field between the IN and SS cases (cf. Fig. 4) may simply reflect the different storm histories for each dataset (cf. Fig. 2). Since most of the storms in the IN database were weak (<50 kt) systems up to 48 h prior to the IOP, the wind field started out from a smaller initial structure. By contrast, most of the storms in the SS database were of hurricane strength as much as 48 h prior to the IOP (and in some cases were of category 4 or 5 intensity). The wind field for SS cases is more likely to be broader, contain greater rainband activity, and potentially have secondary eyewalls (Sitkowski et al. 2011; Rozoff et al. 2012). Structures consistent with these features were seen in the composite mean axisymmetric fields (cf. Figs. 3–6). Furthermore, the reduced azimuthal coverage of reflectivity for SS cases (cf. Figs. 8 and 9) is consistent with the recent finding of Hence and Houze (2012) that inner concentric eyewalls exhibit a greater shear-induced asymmetry than single-eyewall cases. Regardless of the origin of the broader wind fields and greater outer-core vorticity in SS cases, however, the fact remains that the greater inertial stability (and resistance to radial displacements) for these cases constrains the radial mass flux and potential for convective development within the eyewall. In addition, if the higher outer-core vorticity seen in SS cases is associated with greater rainband and/or secondary eyewall activity, that would have implications for the thermodynamic modification of the boundary layer through convective downdrafts.

The lack of a statistically significant difference in the 2–7-km vortex tilt between the IN and SS cases (cf. Fig. 7) is somewhat surprising, since previous observational and modeling studies have indicated an inverse relationship between vertical alignment and intensity change (Zehr 2003; Riemer et al. 2010). However, considering the fact that only TCs of hurricane strength were

included in this database, and the mean intensity of TCs from both IN and SS cases is ~90 kt (cf. Table 2), it is likely that the vortices are already vertically aligned. If weaker TCs (e.g., tropical depressions and storms) were studied, it is likely that larger values of vortex tilt (or displacement) would be observed, particularly for SS cases. Since an inadequate number of cases exist for the Doppler datasets, however, this statement is by necessity speculative and awaits further analysis with more observational or modeling cases.

A key question to ask based on these results is why convective bursts in intensifying TCs tend to be located inside the RMW (cf. Figs. 14 and 15). There are several plausible hypotheses: 1) the reduced inertial stability within the outer core for intensifying cases provides a reduced resistance to radial displacements, allowing for a greater inward radial mass flux that extends inward to smaller radii; 2) related to the first hypothesis, the low-level convergence underneath the eyewall is maximized inside the RMW instead of outside it; and 3) with a greater radial shear of the tangential wind and a ringlike structure to the vorticity field for intensifying cases, the potential for eye–eyewall mixing and regions of localized convergence along the inner edge of the eyewall is enhanced.

Another logical question to ask pertains to the exact role of convective bursts in TC intensification. Broadly put, are convective bursts a cause of TC intensification, or are they simply a reflection of processes occurring within the vortex that provide a favorable local environment for the development of convective bursts? As mentioned above, recent studies documenting the role of diabatic heating in the evolution of the vortex primary and secondary circulation patterns have identified a few ways that convective heating can strengthen a vortex, for example, either through Sawyer–Eliassen-type forcing (e.g., Vigh and Schubert 2009; Pendergrass and Willoughby 2009) or through the warming of the upper levels through convectively induced subsidence (e.g., Heymsfield et al. 2001; Guimond et al. 2010; Zhang and Chen 2012; Chen and Zhang 2013). Such a relationship would suggest that convective bursts are a cause of TC intensification, rather than simply an effect. However, the nature of the dataset analyzed here (i.e., composite means of "snapshots" of individual radial passes and full-flight IOPs) precludes a definitive answer to this question from being found. The question of vacillation cycles [i.e., the transition of the eyewall from symmetric to asymmetric structures (and back) via barotropic instability and vortex Rossby wave propagation] could not be addressed by this dataset either, because of limitations in both the spatial and temporal coverage.

These and other questions will be pursued in future work. Some of the limitations of the Doppler dataset (e.g., coverage limitations and their inability to reliably represent higher-wavenumber asymmetries) will make a rigorous investigation of these questions difficult. Testing with high-resolution numerical models with their more complete spatial coverage and high temporal resolution, will provide the potential to address these questions. This will especially be helpful for assessing the role of convective-scale processes on intensification, since convective features evolve over a much smaller time scale than vortex-scale features. Furthermore, additional cases will be added to the airborne Doppler database to provide greater statistical confidence to the differences discussed here. Additional parameters from the Doppler analyses, such as the distribution of turbulent kinetic energy and vertical profiles at higher vertical resolution to better capture boundary layer structure (e.g., Lorsolo et al. 2010), will also be compared for each dataset. Finally, GPS dropsonde and flight-level data will be added to the database. This should provide information on the difference in the thermodynamic structures of intensifying and steady-state TCs.

APPENDIX

Calculation Methodology for Statistics Shown in Table 3

The methodology used to calculate the statistics to enable a comparison of inner-core structural features between IN and SS cases shown in Table 3 is provided here:

- scaled outer-core tangential wind—tangential wind at 2-km altitude in the $r* = 2$–3 radial band scaled by 2-km tangential wind at $r* = 1$ (dimensionless),
- scaled vertical profile of eyewall tangential wind—ratio of peak tangential wind at 8-km altitude to peak tangential wind at 2-km altitude (dimensionless),
- scaled inner-eyewall vorticity—2-km vorticity at $r* = 0.3$ scaled by vorticity at $r* = 0.6$ (dimensionless).

- scaled outer-core vorticity—2-km vorticity averaged from $r* = 2$ to 3 scaled by vorticity at $r* = 1$ (dimensionless),
- inflow strength—inflow averaged in $z = 0.5$–1-km layer and $r* = 1.5$–2.5 band (m s^{-1}),
- inflow depth—altitude where radial flow from $r* = 1.5$–2.5 is 10% of radial flow from $z = 0.5$–1-km height (km),
- eyewall vertical velocity—vertical velocity in 4–6-km layer in $r* = 0.95$–1.1 band (m s^{-1}), and
- radial location of convective bursts—normalized radius of convective burst (dimensionless).

REFERENCES

Black, M. L., R. W. Burpee, and F. D. Marks Jr., 1996: Vertical motion characteristics of tropical cyclones determined with airborne Doppler radial velocities. *J. Atmos. Sci.,* **53,** 1887–1909.

——, J. F. Gamache, F. D. Marks, C. E. Samsury, and H. E. Willoughby, 2002: Eastern Pacific Hurricanes Jimena of 1991 and Olivia of 1994: The effect of vertical shear on structure and intensity. *Mon. Wea. Rev.,* **130,** 2291–2312.

Braun, S. A., 2002: A cloud-resolving simulation of Hurricane Bob (1991): Storm structure and eyewall buoyancy. *Mon. Wea. Rev.,* **130,** 1573–1592.

——, 2006: High-resolution simulation of Hurricane Bonnie (1998). Part II: Water budget. *J. Atmos. Sci.,* **63,** 43–64.

——, and L. Wu, 2007: A numerical study of Hurricane Erin (2001). Part II: Shear and the organization of eyewall vertical motion. *Mon. Wea. Rev.,* **135,** 1179–1194.

——, M. T. Montgomery, and Z. Pu, 2006: High-resolution simulation of Hurricane Bonnie (1998). Part I: The organization of eyewall vertical motion. *J. Atmos. Sci.,* **63,** 19–42.

Cecil, D. J., E. J. Zipser, and S. W. Nesbitt, 2002: Reflectivity, ice scattering, and lightning characteristics of hurricane eyewalls and rainbands. Part I: Quantitative description. *Mon. Wea. Rev.,* **130,** 769–784.

Chen, H., and D. L. Zhang, 2013: On the rapid intensification of Hurricane Wilma (2005). Part II: Convective bursts and the upper-level warm core. *J. Atmos. Sci.,* **70,** 146–162.

Cram, T. A., J. Persing, M. T. Montgomery, and S. A. Braun, 2007: A Lagrangian trajectory view on transport and mixing processes between the eye, eyewall, and environment using a high-resolution simulation of Hurricane Bonnie (1998). *J. Atmos. Sci.,* **64,** 1835–1856.

Davis, C. A., S. C. Jones, and M. Riemer, 2008: Hurricane vortex dynamics during Atlantic extratropical transition. *J. Atmos. Sci.,* **65,** 714–736.

DeMaria, M., and J. Kaplan, 1999: An updated Statistical Hurricane Intensity Prediction Scheme (SHIPS) for the Atlantic and eastern North Pacific basins. *Wea. Forecasting,* **14,** 326–337.

——, M. Mainelli, L. K. Shay, J. A. Knaff, and J. Kaplan, 2005: Further improvements to the Statistical Hurricane Intensity Prediction Scheme (SHIPS). *Wea. Forecasting,* **20,** 531–543.

Eastin, M. D., W. M. Gray, and P. G. Black, 2005: Buoyancy of convective vertical motions in the inner core of intense hurricanes. Part II: Case studies. *Mon. Wea. Rev.,* **133,** 209–227.

Emanuel, K. A., 1986: An air–sea interaction theory for tropical cyclones. Part I: Steady-state maintenance. *J. Atmos. Sci.,* **43,** 585–605.

Gamache, J. F., 1997: Evaluation of a fully three-dimensional variational Doppler analysis technique. Preprints, *28th Conf. on Radar Meteorology,* Austin, TX, Amer. Meteor. Soc., 422–423.

Gao, J., M. Xue, A. Shapiro, and K. K. Droegemeier, 1999: A variational method for the analysis of three-dimensional wind fields from two Doppler radars. *Mon. Wea. Rev.,* **127,** 2128–2142.

Gentry, R. C., T. T. Fujita, and R. C. Sheets, 1970: Aircraft, spacecraft, satellite and radar observations of Hurricane Gladys, 1968. *J. Appl. Meteor.,* **9,** 837–850.

Guimond, S. R., G. M. Heymsfield, and F. J. Turk, 2010: Multiscale observations of Hurricane Dennis (2005): The effects of hot towers on rapid intensification. *J. Atmos. Sci.,* **67,** 633–654.

Hence, D. A., and R. A. Houze Jr., 2008: Kinematic structure of convective-scale elements in the rainbands of Hurricanes Katrina and Rita (2005). *J. Geophys. Res.,* **113,** D15108, doi:10.1029/2007JD009429.

——, and ——, 2012: Vertical structure of tropical cyclones with concentric eyewalls as seen by the TRMM Precipitation Radar. *J. Atmos. Sci.,* **69,** 1021–1036.

Hendricks, E. A., M. T. Montgomery, and C. A. Davis, 2004: The role of "vortical" hot towers in the formation of Tropical Cyclone Diana (1984). *J. Atmos. Sci.,* **61,** 1209–1232.

——, M. S. Peng, B. Fu, and T. Li, 2010: Quantifying environmental control on tropical cyclone intensity change. *Mon. Wea. Rev.,* **138,** 3243–3271.

Hennon, P. A., 2006: The role of the ocean in convective burst initiation: Implications for tropical cyclone intensification. Ph.D. dissertation, The Ohio State University, 185 pp.

Heymsfield, G. M., J. B. Halverson, J. Simpson, L. Tian, and T. P. Bui, 2001: ER-2 Doppler radar investigations of the eyewall of Hurricane Bonnie during the Convection and Moisture Experiment-3. *J. Appl. Meteor.,* **40,** 1310–1330.

Houze, R. A., Jr., F. D. Marks Jr., and R. A. Black, 1992: Dual-aircraft investigation of the inner core of Hurricane Norbert. Part II: Mesoscale distribution of ice particles. *J. Atmos. Sci.,* **49,** 943–963.

——, W.-C. Lee, and M. M. Bell, 2009: Convective contribution to the genesis of Hurricane Ophelia (2005). *Mon. Wea. Rev.,* **137,** 2778–2800.

Jiang, H., 2012: The relationship between tropical cyclone intensity change and the strength of inner-core convection. *Mon. Wea. Rev.,* **140,** 1164–1176.

Jordan, C. L., 1958: Mean soundings for the West Indies area. *J. Atmos. Sci.,* **15,** 91–97.

Jorgensen, D. F., 1984: Mesoscale and convective-scale characteristics of mature hurricanes. Part I: General observations by research aircraft. *J. Atmos. Sci.,* **41,** 1268–1286.

——, E. J. Zipser, and M. A. LeMone, 1985: Vertical motions in intense hurricanes. *J. Atmos. Sci.,* **42,** 839–856.

Kaplan, J., M. DeMaria, and J. A. Knaff, 2010: A revised tropical cyclone rapid intensification index for the Atlantic and eastern North Pacific basins. *Wea. Forecasting,* **25,** 220–241.

Kelley, O. A., J. Stout, and J. B. Halverson, 2004: Tall precipitation cells in tropical cyclone eyewalls are associated with tropical cyclone intensification. *Geophys. Res. Lett.,* **31,** L24112, doi:10.1029/2004GL021616.

Kepert, J. D., 2001: The dynamics of boundary layer jets within the tropical cyclone core. Part I: Linear theory. *J. Atmos. Sci.,* **58,** 2469–2484.

Kieper, M. E., and H. Jiang, 2012: Predicting tropical cyclone rapid intensification using the 37 GHz ring pattern identified from passive microwave measurements. *Geophys. Res. Lett.,* **39,** L13804, doi:10.1029/2012GL052115.

Kossin, J. P., and M. D. Eastin, 2001: Two distinct regimes in the kinematic and thermodynamic structure of the hurricane eye and eyewall. *J. Atmos. Sci.,* **58,** 1079–1090.

——, and W. H. Schubert, 2001: Mesovortices, polygonal flow patterns, and rapid pressure falls in hurricane-like vortices. *J. Atmos. Sci.,* **58,** 2196–2209.

Lorsolo, S., J. Zhang, F. D. Marks, and J. Gamache, 2010: Estimation and mapping of hurricane turbulent energy using airborne Doppler measurements. *Mon. Wea. Rev.,* **138,** 3656–3670.

Malkus, J. S., and H. Riehl, 1960: On the dynamics and energy transformations in steady state hurricanes. *Tellus,* **12,** 1–20.

Marks, F. D., Jr., and R. A. Houze Jr., 1987: Inner core structure of Hurricane Alicia from airborne Doppler radar observations. *J. Atmos. Sci.,* **44,** 1296–1317.

——, and L. K. Shay, 1998: Landfalling tropical cyclones: Forecast problems and associated research opportunities. *Bull. Amer. Meteor. Soc.,* **79,** 305–323.

——, R. A. Houze Jr., and J. F. Gamache, 1992: Dual-aircraft investigation of the inner core of Hurricane Norbert. Part I: Kinematic structure. *J. Atmos. Sci.,* **49,** 919–942.

Montgomery, M. T., and R. J. Kallenbach, 1997: A theory for vortex Rossby waves and its application to spiral bands and intensity changes in hurricanes. *Quart. J. Roy. Meteor. Soc.,* **123,** 435–465.

——, and R. K. Smith, 2012: Paradigms for tropical-cyclone intensification. *Trop. Cyc. Res. Rep.,* **1,** 1–29.

——, V. A. Vladimirov, and P. V. Denissenko, 2002: An experimental study on hurricane mesovortices. *J. Fluid Mech.,* **471,** 1–32.

——, M. Nicholls, T. Cram, and A. Saunders, 2006: A ''vortical'' hot tower route to tropical cyclogenesis. *J. Atmos. Sci.,* **63,** 355–386.

Nguyen, C. M., M. J. Reeder, N. E. Davidson, R. K. Smith, and M. T. Montgomery, 2011: Inner-core vacillation cycles during the intensification of Hurricane Katrina. *Quart. J. Roy. Meteor. Soc.,* **137,** 829–844.

Nolan, D. S., and L. D. Grasso, 2003: Nonhydrostatic, three-dimensional perturbations to balanced, hurricane-like vortices. Part II: Symmetric response and nonlinear simulations. *J. Atmos. Sci.,* **60,** 2717–2745.

——, Y. Moon, and D. P. Stern, 2007: Tropical cyclone intensification from asymmetric convection: Energetics and efficiency. *J. Atmos. Sci.,* **64,** 3377–3405.

Ooyama, K., 1969: Numerical simulation of the life cycle of tropical cyclones. *J. Atmos. Sci.,* **26,** 3–40.

——, 1982: Conceptual evolution of the theory and modeling of the tropical cyclone. *J. Meteor. Soc. Japan,* **60,** 369–380.

Pendergrass, A. G., and H. E. Willoughby, 2009: Diabatically induced secondary flows in tropical cyclones. Part I: Quasi-steady forcing. *Mon. Wea. Rev.,* **137,** 805–821.

Persing, J., and M. T. Montgomery, 2003: Hurricane superintensity. *J. Atmos. Sci.,* **60,** 2349–2371.

Reasor, P. D., and M. D. Eastin, 2012: Rapidly intensifying Hurricane Guillermo (1997). Part II: Resilience in shear. *Mon. Wea. Rev.,* **140,** 425–444.

——, M. T. Montgomery, F. D. Marks Jr., and J. F. Gamache, 2000: Low-wavenumber structure and evolution of the hurricane inner core observed by airborne dual-Doppler radar. *Mon. Wea. Rev.,* **128,** 1653–1680.

——, ——, and L. D. Grasso, 2004: A new look at the problem of tropical cyclones in vertical shear flow: Vortex resiliency. *J. Atmos. Sci.,* **61,** 3–22.

——, M. D. Eastin, and J. F. Gamache, 2009: Rapidly intensifying Hurricane Guillermo (1997). Part I: Low-wavenumber structure and evolution. *Mon. Wea. Rev.,* **137,** 603–631.

——, R. F. Rogers, and S. Lorsolo, 2013: Environmental flow impacts on tropical cyclone structure diagnosed from airborne Doppler radar composites. *Mon. Wea. Rev.,* **141,** 2949–2969.

Riemer, M., M. T. Montgomery, and M. E. Nicholls, 2010: A new paradigm for intensity modification of tropical cyclones: Thermodynamic impact of vertical wind shear on the inflow layer. *Atmos. Chem. Phys.,* **10,** 3163–3188.

Rodgers, E. B., W. S. Olson, V. M. Karyampudi, and H. F. Pierce, 1998: Satellite-derived latent heating distribution and environmental influences in Hurricane Opal (1995). *Mon. Wea. Rev.,* **126,** 1229–1247.

Rogers, R. F., 2010: Convective-scale structure and evolution during a high-resolution simulation of tropical cyclone rapid intensification. *J. Atmos. Sci.,* **67,** 44–70.

——, S. S. Chen, J. Tenerelli, and H. E. Willoughby, 2003: A numerical study of the impact of vertical shear on the distribution of rainfall in Hurricane Bonnie (1998). *Mon. Wea. Rev.,* **131,** 1577–1599.

——, and Coauthors, 2006: The Intensity Forecasting Experiment (IFEX): A NOAA multiyear field program for improving tropical cyclone intensity forecasts. *Bull. Amer. Meteor. Soc.,* **87,** 1523–1537.

——, M. L. Black, S. S. Chen, and R. A. Black, 2007: An evaluation of microphysics fields from mesoscale model simulations of tropical cyclones. Part I: Comparisons with observations. *J. Atmos. Sci.,* **64,** 1811–1834.

——, F. D. Marks Jr., and T. Marchok, 2009: Tropical cyclone rainfall. *Encyclopedia of Hydrological Sciences,* M. G. Anderson, Ed., John Wiley and Sons, doi:10.1002/0470848944.hsa030.

——, S. Lorsolo, P. D. Reasor, J. Gamache, and F. D. Marks Jr., 2012: Multiscale analysis of tropical cyclone kinematic structure from airborne Doppler radar composites. *Mon. Wea. Rev.,* **140,** 77–99.

——, and Coauthors, 2013: NOAA's Hurricane Intensity Forecasting Experiment (IFEX): A progress report. *Bull. Amer. Meteor. Soc.,* **94,** 859–882.

Rotunno, R., and K. A. Emanuel, 1987: An air–sea interaction theory for tropical cyclones. Part II: Evolutionary study using a nonhydrostatic axisymmetric numerical model. *J. Atmos. Sci.,* **44,** 542–561.

Rozoff, C. M., D. S. Nolan, J. P. Kossin, F. Zhang, and J. Fang, 2012: The roles of an expanding wind field and inertial stability in tropical cyclone secondary eyewall formation. *J. Atmos. Sci.,* **69,** 2621–2643.

Schubert, W. H., and J. J. Hack, 1982: Inertial stability and tropical cyclone development. *J. Atmos. Sci.,* **39,** 1687–1697.

——, M. T. Montgomery, R. K. Taft, T. A. Guinn, S. R. Fulton, J. P. Kossin, and J. P. Edwards, 1999: Polygonal eyewalls, asymmetric eye contraction, and potential vorticity mixing in hurricanes. *J. Atmos. Sci.,* **56,** 1197–1223.

Simpson, J., J. B. Halverson, B. S. Ferrier, W. A. Petersen, R. H. Simpson, R. Blakeslee, and S. L. Durden, 1998: On the role of ''hot towers'' in tropical cyclone formation. *Meteor. Atmos. Phys.,* **67,** 15–35.

Sitkowski, M., J. P. Kossin, and C. M. Rozoff, 2011: Intensity and structure changes during hurricane eyewall replacement cycles. *Mon. Wea. Rev.,* **139,** 3829–3847.

Smith, R. K., M. T. Montgomery, and H. Zhu, 2005: Buoyancy in tropical cyclones and other rapidly rotating atmospheric vortices. *Dyn. Atmos. Oceans,* **40,** 189–208.

——, ——, and N. V. Sang, 2009: Tropical cyclone spin up revisited. *Quart. J. Roy. Meteor. Soc.,* **135,** 1321–1335.

Squires, K., and S. Businger, 2008: The morphology of eyewall lightning outbreaks in two category 5 hurricanes. *Mon. Wea. Rev.,* **136,** 1706–1726.

Vigh, J. L., and W. H. Schubert, 2009: Rapid development of the tropical cyclone warm core. *J. Atmos. Sci.,* **66,** 3335–3350.

Yuter, S. E., and R. A. Houze, 1995: Three-dimensional kinematic and microphysical evolution of Florida cumulonimbus. Part II: Frequency distributions of vertical velocity, reflectivity, and differential reflectivity. *Mon. Wea. Rev.,* **123,** 1941–1963.

Zehr, R. M., 2003: Environmental vertical wind shear with Hurricane Bertha (1996). *Wea. Forecasting,* **18,** 345–356.

Zhang, D.-L., and H. Chen, 2012: Importance of the upper-level warm core in the rapid intensification of a tropical cyclone. *Geophys. Res. Lett.,* **39,** L02806, doi:10.1029/2011GL050578.

Zhang, J. A., R. F. Rogers, D. S. Nolan, and F. D. Marks Jr., 2011: On the characteristic height scales of the hurricane boundary layer. *Mon. Wea. Rev.,* **139,** 2523–2535.